Title
Proton-induced reactions on Fe, Cu, and Ti from threshold to 55 MeV

Journal
The European Physical Journal A, 57(3)

ISSN
1434-6001

Authors
Voyles, Andrew S
Lewis, Amanda M
Morrell, Jonathan T
et al.

Publication Date
2021-03-01

DOI
10.1140/epja/s10050-021-00401-2

Peer reviewed

Eur. Phys. J. A (2021) 57:94
https://doi.org/10.1140/epja/s10050-021-00401-2

THE EUROPEAN PHYSICAL JOURNAL A

Regular Article - Experimental Physics

Proton-induced reactions on Fe, Cu, and Ti from threshold to 55 MeV

Andrew S. Voyles[1,a], **Amanda M. Lewis**[1], **Jonathan T. Morrell**[1], **M. Shamsuzzoha Basunia**[2], **Lee A. Bernstein**[1,2], **Jonathan W. Engle**[3], **Stephen A. Graves**[4], **Eric F. Matthews**[1]

[1] Department of Nuclear Engineering, University of California, Berkeley, Berkeley, CA 94720, USA
[2] Nuclear Science Division, Lawrence Berkeley National Laboratory, Berkeley, CA 94720, USA
[3] Department of Medical Physics, University of Wisconsin – Madison, Madison, WI 53705, USA
[4] Department of Radiology, University of Iowa, Iowa City, IA 52242, USA

Received: 3 January 2020 / Accepted: 15 February 2021 / Published online: 15 March 2021

Communicated by Jose Benlliure

Abstract Theoretical models often differ significantly from measured data in their predictions of the magnitude of nuclear reactions that produce radionuclides for medical, research, and national security applications. In this paper, we compare *a priori* predictions from several state-of-the-art reaction modeling packages (CoH, EMPIRE, TALYS, and ALICE) to cross sections measured using the stacked-target activation method. The experiment was performed using the Lawrence Berkeley National Laboratory 88-Inch Cyclotron with beams of 25 and 55 MeV protons on a stack of iron, copper, and titanium foils. Thirty-four excitation functions were measured from 4–55 MeV, including the first measurement of the independent cross sections for ^{nat}Fe(p,x)^{49,51}Cr, ^{51,52m,52g,56}Mn, and ^{58m,58g}Co. All of the models, using default input parameters to assess their predictive capabilities, failed to reproduce the isomer-to-ground state ratio for reaction channels at compound and pre-compound energies, suggesting issues in modeling the deposition or distribution of angular momentum in these residual nuclei.

1 Introduction

Clinical practice of nuclear medicine is rapidly growing with the inclusion of a broader array of radiopharmaceuticals. Future growth is anticipated, given the pre-clinical success of many new and emerging radionuclides. Although the physical and chemical properties of these novel radionuclides tend to be well-established, their broad-scale clinical applications are reliant upon well-characterized nuclear data to facilitate production. One particular set of emerging radionuclides are positron-emitting isotopes of manganese, which have been identified as having potential for a range of diagnostic applications [1–6]. In particular, a significant interest has been expressed in producing the emerging radionuclides ^{51}Mn for clinical use in quantitative positron emission tomography (PET) studies, as well as ^{52g}Mn for pre-clinical imaging of neural and immune processes via PET [7].

Manganese radionuclides are desirable for radiopharmaceutical applications, as they possess well-established biochemistry and have been chelated by the complexing agent DOTA for tracking monoclonal antibodies with high biostability at neutral pH [2]. ^{52}Mn ($t_{1/2}$ = 5.591 ± 0.003 d, I_{β^+} = 29.4%, $E_{\beta,\,avg}$ = 0.242 MeV [8]) has been shown to be useful for immuno-PET applications, offering the possibility for imaging within minutes of injection, making it highly suitable for pre-clinical imaging as a longer-lived complement to the more established immuno-PET agents ^{89}Zr and ^{64}Cu. However, its long half-life and unfavorable high-energy decay gamma-rays make it undesirable for clinical applications. The short half-life of the ^{52m}Mn isomer ($t_{1/2}$ = 21.1 ± 0.2 min) makes production and handling difficult, and with a high-intensity gamma emission (1434.06 keV, I_γ = 98.2 ± 0.5%), ^{52m}Mn is similarly undesirable for clinical applications [8]. In contrast, ^{51}Mn ($t_{1/2}$ = 46.2 ± 0.1 min, I_{β^+} = 96.86%, $E_{\beta,\,avg}$ = 0.964 MeV [4,9]), is more clinically suitable for rapid metabolic studies. ^{51}Mn lacks any strong decay gamma-rays (its longer-lived daughter ^{51}Cr [$t_{1/2}$ = 27.704 ± 0.003 d] has only a single 320.0284 keV [I_γ = 9.910 ± 0.010%] line), making it the best choice of these radionuclides for clinical imaging.

Supplementary Information The online version contains supplementary material available at https://doi.org/10.1140/epja/s10050-021-00401-2.

[a] e-mail: andrew.voyles@berkeley.edu (corresponding author)

Developing production of these radionuclides requires well-characterized cross section data or predictive models when such data have not been measured. Modeling of nuclear reactions in the A=40–70 mass region presents numerous challenges including uncertainties in nuclear level densities as a function of spin due to the opening of the $f_{7/2}$ orbital and the presence of enhanced γ-strength at low energies [10–12]. Therefore, as part of a larger campaign to address deficiencies in cross-cutting nuclear data needs [13], our group has measured the nuclear excitation functions of the radionuclides ^{51}Mn, ^{52m}Mn, and ^{52g}Mn from proton-induced reactions on Fe. We used the thin-foil stacked-target technique to study proton-induced reactions on Fe foils of natural isotopic abundance with Ti and Cu monitor foils. This work complements earlier measurements using 40–100 MeV protons and extends them down to reaction thresholds, to investigate the feasibility of production using the international network of low-energy medical cyclotrons [7]. Furthermore, we used our measured data to probe the role of angular momentum in the transitional energy region between compound and direct reactions since both the ground and long-lived isomeric states in ^{52}Mn were populated.

In addition to their interest for PET studies, the ^{51,52g,52m}Mn excitation functions offer an opportunity to study the distribution of angular momentum in compound nuclear and direct pre-equilibrium reactions via observation of the ^{52m}Mn ($t_{1/2}$ = 21.1 ± 0.2 min; $J^{\pi} = 2^{+}$) to ^{52g}Mn ($t_{1/2}$ = 5.591 ± 0.003 d; $J^{\pi} = 6^{+}$) ratio [8,9]. Measurements of isomer-to-ground state ratios have been used for over 20 years to probe the spin distribution of excited nuclear states in the A ≈ 190 region [14,15]. These measurements also provide an opportunity to benchmark the predictive capabilities of reaction modeling codes used for nuclear reaction evaluations and the way in which they implement the underlying physical reaction mechanisms.

2 Experimental methods and materials

The work described herein follows the methods utilized in our recent work and established by Graves *et al.* for monitor reaction characterization of beam energy and fluence in stacked target irradiations [7,16]. Preliminary results were reported in a Master's thesis [17]; here we report the final analysis of that work. Unless otherwise stated, all values are presented herein as mean ± SD, or as the calculated result ± half the width of a 68% confidence interval.

2.1 Stacked-target design

Two separate irradiations were performed at incident proton energies of 25 and 55 MeV, respectively. We constructed a pair of target stacks for this work, one stack covering the 55–20 MeV range and the other 25–0 MeV. This minimized the systematic uncertainties associated with significant degradation of beam energy, and included multiple overlapping measurements between 20–25 MeV as a consistency check between the stacks. A series of nominal 25 μm ^{nat}Fe foils (99.5%, lot #LS470411), 25 μm ^{nat}Ti foils (99.6%, lot #LS471698), and 25 μm ^{nat}Cu foils (99.95%, lot #LS471698) were used (all from Goodfellow Corporation, Coraopolis, PA 15108, USA) as targets. In each stack, seven foils were cut down to 2.5×2.5 cm squares and spatially characterized at four different locations using a digital caliper and micrometer (Mitutoyo America Corp.). Four mass measurements were performed using an analytical balance in order to determine their areal density. The foils were sealed into "packets" between two pieces of 3M 5413-Series Kapton polyimide film tape, each piece of tape consisting of 43.2 μm of a silicone adhesive (nominal 4.79 mg/cm^2) on 25.4 μm of a polyimide backing (nominal 3.61 mg/cm^2). The sealed foils were mounted over the hollow center of 1.5875 mm-thick aluminum frames. Plates of 6061 aluminum alloy served as proton energy degraders between energy positions. The target box is machined from 6061 aluminum alloy and mounts on the end of a beamline, electrically-isolated for the purposes of current monitoring. The specifications of both target stacks are in Table 6 of Appendix A.

Both target stacks were separately irradiated at the Lawrence Berkeley National Laboratory (LBNL) 88-Inch Cyclotron, a K=140 sector-focused cyclotron [18]. The 25 MeV stack was irradiated for 20 minutes at a nominal current of 100 nA, for an integral current of 31.61 nAh, measured using a current integrator on the electrically-isolated beamline. The 55 MeV stack was irradiated for 10 minutes at a nominal current of 120 nA, for an integral current of 20.78 nAh. The beam current remained stable under these conditions for the duration of each irradiation. The approximately 1 cm-diameter proton beam incident upon each stack's upstream stainless steel profile monitor had a maximum energy of either 25 or 55 MeV, with an approximately 2% energy width due to multi-turn extraction — these energy profiles were used for all later analysis. Following end-of-bombardment (EOB), each stack was removed from the beamline and disassembled. All activated foils were transported to a counting lab for gamma spectrometry, which started approximately 20 minutes following the end of each irradiation.

2.2 Quantification of induced activities

A single ORTEC GMX Series (model #GMX-50220-S) High-Purity Germanium (HPGe) detector was used to determine the activities in each target. Samples were counted at fixed positions ranging 5–60 cm (5% maximum permissible dead-time) from the front face of the detector. The foils were

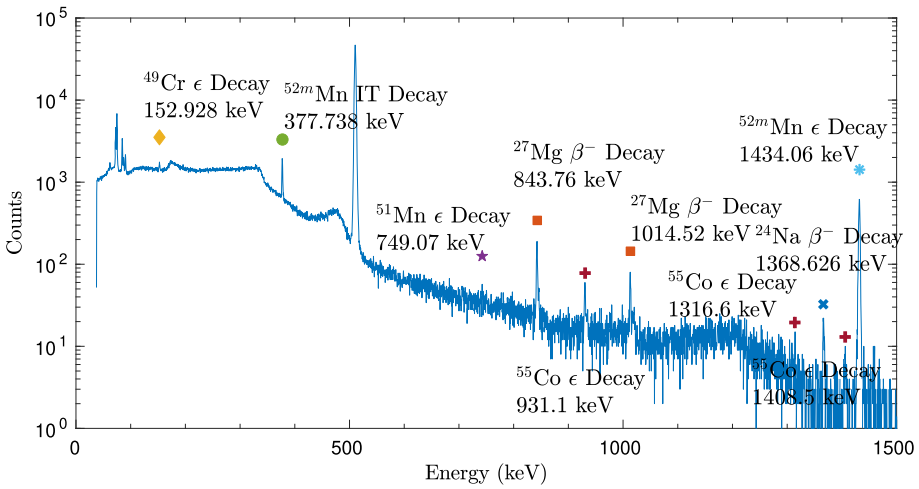

Fig. 1 A gamma spectrum from an activated Fe foil at approximately 55 MeV (the maximum incident proton energy), collected 25 min after end-of-bombardment. Several observed reaction products are visible in this spectrum, and the ^{51}Mn and ^{52m}Mn decay lines, which form two of the primary reaction channels of interest, are clearly isolated from surrounding peaks

counted for 4 weeks following EOB. An example of one of the gamma-ray spectra collected is shown in Fig. 1. Net peak areas were fitted using the code FitzPeaks [19], which utilizes the SAMPO fitting algorithms for gamma-ray spectra [20].

The net counts in each fitted gamma-ray photopeak were converted into activities for the decaying activation products. The half-lives and gamma-ray branching ratios used for all calculations of measured cross sections reported in this work have been taken from the most recent edition of Nuclear Data Sheets for each mass chain [4,8,9,21–36]. Corrections (typically <0.2%) for gamma-ray attenuation within each foil packet were made, using photon attenuation coefficients from the XCOM photon cross sections database [37]. EOB activities were determined by χ^2-fitting of all observed decay gammas for a product to the decay curve. The total uncertainty in activity is the propagated sum of the uncertainty in fitted peak areas, uncertainty in detector efficiency calibration, uncertainty in the gamma-ray branching ratio data, and uncertainty in photon attenuation coefficients (taken as 5%).

As in our previous work, these activities were used to calculate cumulative and independent cross sections [16]. For the first product nuclide in a mass chain with observable decay gammas, its (p,x) cross section is reported as a cumulative cross section (σ_c), which is the sum of direct production of that nucleus, as well as decay of its precursors and any other independent cross sections leading to that nucleus. Cumulative cross sections are reported whenever it is impossible to use decay spectrometry to distinguish independent production of a nucleus from decay feeding. For all remaining observed reaction products in the mass chain, and cases where no decay precursors exist, independent cross sections (σ_i) corresponding to a single residual product are reported, facilitating comparison to reaction model calculations. Solutions to the first- and higher-order Bateman equations are used for separation of feeding contributions from decay precursors so that independent cross sections may be reported [38,39].

2.3 Proton fluence determination

Thin ^{nat}Ti and ^{nat}Cu foils were co-irradiated to measure beam current at each position within the stack. The International Atomic Energy Agency (IAEA)-recommended ^{nat}Ti(p,x)^{46}Sc, ^{nat}Ti(p,x)^{48}V, ^{nat}Cu(p,x)^{62}Zn, and ^{nat}Cu(p,x)^{63}Zn monitor reactions were used [40]. Systematically enhanced fluence from ^{nat}Ti(p,x)^{48}Sc co-production was avoided by only using the 928.327, 944.130, and 2240.396 keV decay gammas from ^{48}V. Using the formalism outlined in our previous work, the integral form of the well-known activation equation was used to determine proton fluence ($I\Delta t$), in order to account for energy loss across each monitor foil [16]. The propagated uncertainty in proton fluence is calculated as the quadrature sum of (1) the uncertainty in quantified EOB activity, (2) uncertainty in the duration of irradiation (conservatively estimated at 10 s, to account for any transient changes in beam current), (3) uncertainty in foil areal density, (4) uncertainty in monitor product half-life (included, but normally negligible), (5) uncertainty in IAEA recommended cross section (using values from the 2017 IAEA re-evaluation [40]), and (6) uncertainty in differential proton fluence (from transport simulations).

2.4 Proton transport calculations

Estimates of the proton beam energy for preliminary stack designs were calculated using the Anderson & Ziegler (A&Z) stopping power formalism [41–43]. However, the transport code FLUKA-2011.2x.3 was used for simulation of the full 3-D target stack and to determine the full proton energy and fluence distribution for each foil [44]. All FLUKA simulations used 10^8 source protons, yielding a statistical uncertainty of less than 0.01%. As with the determination of pro-

ton fluence in the monitor foils, the progressively increasing energy straggle towards the rear of each stack is accounted for using FLUKA. These energy distributions $\frac{d\phi}{dE}$ were used to calculate a flux-weighted average proton energy $\langle E \rangle$, which accounts for the slowing-down of protons within a foil (particularly in the low-energy stack) and reports the effective energy centroid for each foil. To report a complete description of the representative energy for each foil, a bin width is provided through the energy uncertainty, calculated as the full width at half maximum (FWHM) of the FLUKA-modeled energy distribution for each foil.

The "variance minimization" techniques utilized in our recent work and established by Graves *et al.* have been used here to reduce uncertainty in proton fluence assignments due to poorly-characterized stopping power [7,16]. This method is based on the assumption that the independent measurements of proton fluence from the different monitor reactions should all be consistent at each position. This disagreement is minor at the front of the stack, but gets progressively worse as the beam travels through the stack due to the compounded effect of systematic errors. As in our prior work, variance minimization treats the effective density of a sensitive set of stack components (such as degraders) as a free parameter in proton transport calculations, to optimize agreement with the IAEA-recommended charged particle monitor standards. Across multiple iterations of these simulations, this parameter is uniformly varied to find the energy spectra for each foil which minimizes the standard deviation of the multiple measurements of proton fluence in a stack compartment. The lowest energy position of a stack is often chosen for this, as it is the most sensitive to perturbations of the transport calculations. It is important to note that this technique does not imply that the measured density of the stack components is incorrect – rather, it is used as a surrogate to correct for poorly-characterized stopping power and other systematic uncertainties.

When performing a variance minimization, it is important to apply this variation of effective areal density to the stack components which have the most significant impact on beam energy loss. Therefore, the aluminum degraders are used for variance minimization for the 55 MeV stack as they make up more than 80% of the areal density of the stack. For the 25 MeV stack, the Kapton tape was chosen for variance minimization as the foil packets themselves are responsible for the majority of beam degradation. While it only makes up approximately 20% of the low-energy stack's areal density, the Kapton surrounding each foil packet has a greater areal density than the foil itself. In addition, it is far easier to directly characterize the areal density of the metallic foils than it is for the Kapton, resulting in only an approximate value for the latter. The contributions to the slowing of the beam due to the tape's adhesive have often been neglected in much work performed to date. This is of relatively minor consequence for higher-energy irradiations (especially relative to any beam degraders), but becomes increasingly important for proton energies below 25 MeV, causing as much as an additional loss of 8 MeV by the time it reaches the end of the stack.

In performing the minimization, the areal density of each of the aluminum degraders (for the 55 MeV stack) was varied uniformly in FLUKA simulations by a factor of up to ±25% of measured values to find the effective density which minimized variance in the measured proton fluence for the four monitor reactions at the lowest energy position (Ti-07, Cu-07). For the 25 MeV stack, the areal density reached in the minimization of the 55 MeV stack was used for the E-09 and H-01 aluminum degraders and the areal density of each of the Kapton tape layers (both adhesive and backing) was varied by ±25%, to find the effective density which minimized variance in the measured proton fluence for the two monitor reactions at the next-to-lowest energy position (Ti-19, Cu-19). These positions were chosen as minimization candidates as they are the most sensitive to systematic uncertainties in stack design. In the 25 MeV stack, activity was not seen in gamma spectrometry for the lowest-energy (Cu-20) monitor foil, implying that the beam was stopped at some point in between Ti-20 and Cu-20. This observation indicates that the stopping power characterization for the stack components (primarily for the difficult-to-characterize Kapton tape) is significantly underestimated, as transport calculations using nominal areal densities predict that the beam should exit the stack with an energy of approximately 7 MeV. As a result, this position was not used for minimization, with the Ti-19 and Cu-19 position being the lowest-energy reliable monitor foils in the stack.

The results of the minimization technique indicate a clear minimum in proton fluence variance for flux-weighted average 22.71 MeV protons entering the last energy position of the 55 MeV stack. This is approximately 2 MeV lower than the nominal FLUKA simulations, which used the 2.68 g/cm^3 measured density of the aluminum degraders. This energy corresponds to an aluminum areal density 4.43% greater than measurements and corrects for stopping power characterization and other minor systematic uncertainties in stack design. Similarly, for the 25 MeV stack, variance minimization converges on flux-weighted average 9.23 MeV protons entering the Fe-13/Ti-19/Cu-19 energy position, which is approximately 4 MeV lower than the nominal FLUKA simulations. This energy corresponds to a Kapton tape areal density of 5.69% greater than nominal measurements, which is completely reasonable given the lack of areal density data from the manufacturer. The impact of this variance minimization for improving disagreement in proton fluence is clearly seen in Fig. 2.

The correlated uncertainty-weighted mean for the two ^{nat}Cu(p,x) and two ^{nat}Ti(p,x) monitor channels was calcu-

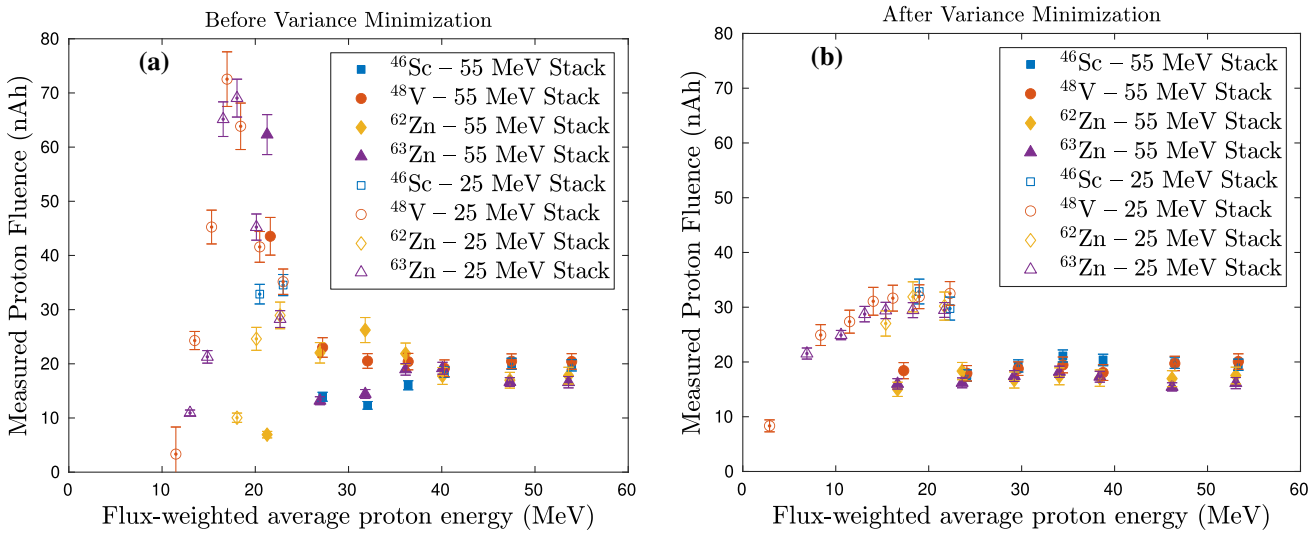

Fig. 2 Proton fluence at various positions in both the 55 MeV and 25 MeV target stacks as determined by the Ti and Cu monitor foils before (left) and after (right) variance minimization. Open data points represent the 25 MeV stack, and filled data points represent the 55 MeV stack. The abrupt change in the post-minimization value at the energies where the two stacks overlap can be attributed to the relatively large energy straggle at the back of the high energy stack

lated at each energy position, to determine the final fluence assignments for the Cu and Ti foils, respectively, and the correlated uncertainty-weighted mean for all four monitor channels was used to determine the final fluence assignments for the Fe foils. This correlated uncertainty-weighted mean was calculated as:

$$\langle I \rangle = \frac{\sum_{i,j} I_j \left(\mathbf{V}_{ij}^{-1}\right)}{\sum_{i,j} \left(\mathbf{V}_{ij}^{-1}\right)} \tag{1}$$

Uncertainty in each final proton fluence is calculated by error propagation of the individual monitor channel fluence values at each energy position:

$$\delta_{\langle I \rangle} = \sqrt{\frac{1}{\sum_{i,j} \left(\mathbf{V}_{ij}^{-1}\right)}} \tag{2}$$

Each element ij of the covariance matrix is calculated using the robust sandwich estimator [45]:

$$\mathbf{V}_{ij} = \mathrm{Cov}[I_i, I_j] = \sum_{\beta} \frac{\partial I}{\partial \beta_i} \delta_{\beta_i} \mathrm{Corr}[\beta_i, \beta_j] \delta_{\beta_j} \frac{\partial I}{\partial \beta_j} \tag{3}$$

where i and j are the monitor reactions in a given compartment, and $\beta \in [A_0,\ \rho\Delta r,\ \lambda,\ \Delta t_{irr},\ \int \sigma(E)\frac{d\phi}{dE}dE]$. A_0 is assumed to be 30% correlated for all reactions, $\rho\Delta r$ is assumed to be 100% correlated for reactions from the same monitor foil, λ is assumed to be uncorrelated, Δt_{irr} is assumed to be 100% correlated, and $\int \sigma(E)\frac{d\phi}{dE}dE$ is assumed to be 30% correlated for reactions from the same monitor foil.

2.5 Calculation of measured cross sections

Using the quantified EOB activities along with the variance-minimized proton fluence, it is possible to calculate cross sections for observed (p,x) reactions. While thin (≈ 10–20 mg/cm^2) foils were irradiated to minimize the energy bins of these cross section measurements, all cross sections reported here are flux-averaged over the energy distribution subtended by each foil. The beam current, measured using a current integrator connected to the electrically-isolated target box, remained stable for the duration of the irradiation. The propagated uncertainty in cross section is calculated as the quadrature sum of the uncertainty in quantified EOB activity (which includes uncertainty in detector efficiencies), uncertainty in the duration of irradiation (conservatively estimated at 10 s, to account for any minor transient changes in beam current), uncertainty in foil areal density, uncertainty in monitor product half-life (included, but normally negligible), and uncertainty in proton current (quantified by error propagation of the monitor reaction fluence values at each energy position).

3 Results and discussion

After irradiation, all foils were still sealed in their Kapton packets, verifying that no activation products were lost due

to packet failure. With the exception of a single foil (Cu-20, in the 25 MeV stack), each activated foil had a small "blister" under the Kapton tape layer caused by a combination of off-gassing of oxides and the formation of gaseous short-lived beta activities in the tape. This blister verifies that the primary proton beam was incident upon the foil, and provides additional evidence that the beam was stopped in the stack between Ti-20 and Cu-20.

Using the final proton fluence at each energy position, cross sections for ^{48,49,51}Cr, ^{48}V, ^{51,52m,52g,52,54,56}Mn, ^{52}Fe, and ^{55,56,57,58m,58g,58}Co were extracted for (p,x) reactions on ^{nat}Fe foils up to 55 MeV, presented in Table 1. For (p,x) reactions on ^{nat}Cu, the (p,x) cross sections for ^{54}Mn, ^{57}Ni, ^{57,60,61}Co, and ^{60,61,64}Cu were extracted, presented in Table 2. For (p,x) reactions on ^{nat}Ti, the (p,x) cross sections for ^{43}K and ^{44g,44m,44,47,48}Sc were extracted, presented in Table 3. In addition, as there exist a number of isomers with unstable ground states in these mass regions, independent measurements of isomer-to-ground-state branching ratios for ^{nat}Fe(p,x)$^{52m/g}$Mn, ^{nat}Fe(p,x)$^{58m/g}$Co, and ^{nat}Ti(p,x)$^{44m/g}$Sc were extracted and are presented in Table 4. The propagated uncertainty in these cross sections varies widely based on the reaction product in question, with the major components arising from uncertainty in EOB activity (±3–10%), proton fluence (±5–13%), and foil areal density (±0.1–0.3%).

The measured cross sections were compared to the predictions by the reaction codes TALYS, EMPIRE, CoH, ALICE, and by the calculations in the TENDL database. The codes were all explicitly run using their default parameters. In contrast, TENDL was developed through a parameter optimization process, and is routinely used for modeling cross sections in initial target designs for isotope production applications. Our recent work has shown that arbitrary parameter optimization (tuning to provide a best fit to a single reaction channel) often provides non-unique solutions, causing neighboring reaction channels (e.g., (p,4n) vs. (p,p3n)), to suffer [46]. A full optimization of the reaction modeling is beyond the scope of this paper. However, a comparison between measured, evaluated, and default calculations for the major channel cross sections serves to highlight the relative fidelity of all three approaches. The default settings for the level density models, optical models, and gamma strength function (γSF) are listed in Table 5. It should be noted that the use of natural abundance targets in these measurements exacerbates the modeling challenges seen in our previous work using monoisotopic targets [16] due to the larger number of reaction channels that can contribute to the production of any given residual nucleus. As a result, this analysis is useful for a qualitative comparison of default predictive capabilities, but no firm conclusions can be drawn about the direct causes of any inaccuracies, as there are many "moving parts" in these calculations.

These results have several notable features. The ^{nat}Fe(p,x), ^{nat}Cu(p,x), and ^{nat}Ti(p,x) cross sections measured here are in excellent agreement with literature, but have been measured nearly exclusively with the highest precision to date. While (p,x) reactions below 70 MeV on these elements are well-characterized overall, measurements of several reaction channels are somewhat sparse in comparison. Indeed, fewer than four existing measurements have been performed for the ^{nat}Fe(p,x)^{48}Cr,^{52}Fe, ^{nat}Cu(p,x)^{60}Cu,^{61}Co, and ^{nat}Ti(p,x)^{44}Sc reactions presented here. Additionally, ^{22,24}Na activity is seen in all foils, consistent with proton activation of the trace silicon in the Kapton tape used for foil encapsulation, as described in our previous work [16]. This serves as another example of how the use of silicone-based adhesives may systematically enhance the apparent fluence if one were to use the ^{nat}Al(p,x)^{22,24}Na monitor reactions. Discussion of notable reaction channels follows here and comparisons of the remaining measured cross sections with modeling results and literature data (retrieved from EXFOR [64]) are seen in the Fig. 1. Physical yield curves have additionally been calculated from logarithmic interpolation of the excitation functions presented in this work, as seen in Fig. 3. All yields are specified in the recommended units of MBq/C [63] and represent the instantaneous production rates. These curves show that production of medically-valuable radionuclides at low-to-intermediate energies by ^{nat}Fe(p,x) is potentially viable, but is dependent upon the required radionuclidic purity on a case-by-case basis.

3.1 ^{nat}Fe(p,x)^{51}Mn cross section

This work presents the first measurement of the ^{nat}Fe(p,x)^{51}Mn reaction in this energy region. However, below the 24.1 MeV threshold for ^{56}Fe(p,x)^{51}Mn, the single measurement of ^{54}Fe(p,x)^{51}Mn from Levkovski can be renormalized by isotopic abundance (and an additional -18% due to an error in the monitor data adopted in the measurement), and is consistent with the present work [65]. For the ^{nat}Fe(p,x)^{51}Mn reactions, seen in Fig. 4, the lower-energy ^{54}Fe(p,α)^{51}Mn reaction, which peaks around 15 MeV, is well-modeled by TALYS and TENDL and over-predicted by the default calculation performed with EMPIRE, CoH, and ALICE. Interestingly, the higher-energy reactions on the higher mass Fe isotopes are better matched by EMPIRE and CoH. ALICE overpredicts the production of ^{51}Mn in both peaks and appears to peak at too high an energy. As was seen in the modeling of high-energy proton-induced niobium reactions [16], TALYS and TENDL do well with the lower-energy "compound" reactions but do not accurately predict the higher-energy reactions that have a significant pre-equilibrium component. The untuned EMPIRE and CoH seem to accurately predict the locations of the peaks, but often fail to reliably estimate the magnitude of the cross section.

Table 1 Measured cross sections for the various ^{nat}Fe(p,x) reaction products observed in this work. Cumulative cross sections are designated as σ_c, independent cross sections are designated as σ_i. Uncertainties are listed in the least significant digit, that is, 131.0(85) mb means 131.0 ± 8.5 mb. Stack ID specifies which irradiation each measurement belongs to – Stack "A" designates the 55 MeV irradiation, Stack "B" designates the 25 MeV irradiation

	Production cross section (mb)													
E_p (MeV)	53.45(61)	46.63(68)	38.93(78)	34.62(85)	29.84(96)	24.4(11)	22.71(43)	19.36(56)	17.6(15)	16.54(48)	14.52(49)	12.11(53)	9.23(61)	4.10(73)
Stack ID	A	A	A	A	A	A	B	B	A	B	B	B	B	B
^{48}Cr(σ_c)	0.172(11)	0.01376(80)	0.00435(29)	–	–	–	–	–	–	–	–	–	–	–
^{48}V(σ_i)	6.38(43)	4.64(29)	0.513(35)	0.1096(80)	–	–	–	–	–	–	–	–	–	–
^{48}V(σ_c)	6.55(43)	4.65(29)	0.517(35)	0.1096(80)	–	–	–	–	–	–	–	–	–	–
^{49}Cr(σ_c)	1.83(12)	2.25(18)	1.20(11)	0.315(36)	–	–	–	–	–	–	–	–	–	–
^{51}Mn(σ_c)	12.02(75)	16.02(96)	12.03(78)	6.28(42)	0.484(40)	0.693(48)	1.083(65)	2.01(15)	2.14(17)	2.02(19)	1.49(14)	0.595(42)	–	–
^{51}Cr(σ_i)	65.4(58)	80.3(58)	56.0(45)	27.3(23)	3.81(35)	0.87(12)	0.65(12)	0.071(49)	0.019(25)	–	–	–	–	–
^{51}Cr(σ_c)	77.4(58)	96.4(59)	68.0(44)	33.6(24)	4.29(35)	1.57(11)	1.74(12)	2.08(13)	2.16(16)	2.02(19)	1.49(14)	0.595(42)	–	–
^{52}Fe(σ_c)	2.74(17)	1.82(11)	1.60(10)	2.25(15)	0.770(52)	0.206(15)	0.192(13)	0.01297(75)	0.00242(21)	–	–	–	–	–
^{52m}Mn(σ_i)	8.29(52)	9.49(54)	13.69(88)	17.9(12)	23.3(15)	11.82(74)	5.78(33)	0.0763(44)	0.0763(57)	0.0754(61)	0.0585(52)	–	–	–
^{52g}Mn(σ_i)	11.58(72)	13.46(76)	20.8(13)	28.2(18)	21.8(15)	16.3(10)	10.37(64)	0.300(17)	0.1124(85)	0.0428(38)	0.00540(50)	–	–	–
^{52g}Mn(σ_c)	13.66(90)	15.6(11)	23.0(18)	30.9(21)	31.7(22)	18.5(13)	10.57(62)	0.313(19)	0.0393(45)	0.0556(48)	0.0185(19)	–	–	–
^{54}Mn(σ_i)	131.0(85)	162(10)	167(12)	129(10)	42.2(34)	2.46(25)	1.10(13)	1.09(14)	1.47(17)	1.53(16)	1.36(12)	1.133(80)	0.747(75)	0.0600(80)
^{55}Co(σ_i)	9.43(63)	12.5(10)	15.7(12)	21.5(15)	48.4(36)	64.7(56)	61.0(45)	43.6(30)	33.6(34)	13.4(12)	0.377(35)	0.0421(29)	–	–
^{56}Mn(σ_c)	–	0.518(39)	0.610(44)	0.462(45)	0.506(54)	0.405(33)	0.223(13)	0.0962(56)	0.0329(43)	0.0253(21)	0.0132(14)	–	–	–
^{56}Co(σ_i)	13.0(11)	16.3(14)	18.9(16)	23.6(17)	29.2(26)	47.8(32)	51.6(30)	82.6(50)	176(13)	197(16)	344(30)	376(24)	288(29)	3.54(47)
^{57}Co(σ_i)	–	0.476(47)	0.539(60)	0.648(44)	1.170(90)	1.84(12)	2.36(14)	2.50(16)	3.20(25)	3.40(28)	5.14(47)	8.18(52)	11.5(12)	5.49(73)
^{58m}Co(σ_i)	–	–	–	0.0427(28)	0.0619(42)	0.1054(69)	0.172(11)	0.236(15)	0.241(19)	0.300(28)	0.475(44)	0.545(35)	0.477(49)	0.170(25)
^{58g}Co(σ_i)	–	–	–	0.0884(66)	0.0980(74)	0.1118(82)	0.1229(84)	0.1484(90)	0.333(28)	0.318(27)	0.919(90)	1.276(96)	1.56(17)	0.623(83)
^{58g}Co(σ_c)	–	–	–	0.1311(72)	0.1599(86)	0.217(11)	0.295(14)	0.384(18)	0.574(34)	0.618(39)	1.39(10)	1.82(10)	2.04(18)	0.792(86)

Table 2 Measured cross sections for the various ^{nat}Cu(p,x) reaction products observed in this work. Cumulative cross sections are designated as σ_c, independent cross sections are designated as σ_i. Uncertainties are listed in the least significant digit, that is, 51.9(34) mb means 51.9 ± 3.4 mb. Stack ID specifies which irradiation each measurement belongs to – Stack "A" designates the 55 MeV irradiation, Stack "B" designates the 25 MeV irradiation

	Production cross section (mb)													
E_p (MeV)	53.04(61)	46.18(68)	38.42(79)	34.06(86)	29.21(97)	23.6(12)	21.70(33)	18.30(38)	16.6(15)	15.38(44)	13.11(49)	10.57(57)	6.90(82)	1.4(13)
Stack ID	A	A	A	A	A	A	B	B	A	B	B	B	B	B
^{54}Mn (σ_i)	2.09(13)	0.428(24)	0.0931(61)	0.0517(33)	0.0223(15)	0.0185(12)	–	–	–	–	–	–	–	–
^{57}Ni (σ_c)	2.15(15)	0.775(45)	0.0530(44)	–	–	–	–	–	–	–	–	–	–	–
^{57}Co (σ_i)	49.8(34)	33.8(23)	3.79(42)	1.206(80)	1.67(11)	1.053(72)	0.707(46)	0.264(27)	–	–	–	–	–	–
^{57}Co (σ_c)	51.9(34)	34.6(23)	3.84(42)	1.206(80)	1.67(11)	1.053(72)	0.707(46)	0.264(27)	–	–	–	–	–	–
^{60}Co (σ_c)	9.41(59)	8.08(47)	6.14(40)	3.12(22)	0.794(63)	0.201(17)	0.125(10)	0.0199(22)	–	–	–	–	–	–
^{60}Cu (σ_c)	25.3(16)	16.86(97)	1.46(12)	0.578(38)	–	–	–	–	–	–	–	–	–	–
^{61}Co (σ_c)	4.26(54)	5.98(66)	6.94(62)	6.61(70)	5.94(83)	0.872(81)	0.253(14)	0.1178(69)	0.0415(35)	–	–	–	–	–
^{61}Cu (σ_c)	79.7(51)	106.4(64)	161(11)	155(10)	104.1(72)	6.97(52)	1.84(13)	1.195(80)	0.809(69)	–	–	–	–	–
^{64}Cu (σ_i)	50.9(32)	55.4(32)	58.4(38)	62.4(41)	101.8(68)	145(14)	83.1(47)	57.0(33)	46.4(35)	22.2(18)	–	–	–	–

Table 3 Measured cross sections for the various ^{nat}Ti(p,x) reaction products observed in this work. Cumulative cross sections are designated as σ_c, independent cross sections are designated as σ_i. Uncertainties are listed in the least significant digit, that is, 25.0(24) mb means 25.0 ± 2.4 mb. Stack ID specifies which irradiation each measurement belongs to – Stack "A" designates the 55 MeV irradiation, Stack "B" designates the 25 MeV irradiation

	Production cross section (mb)													
E_p (MeV)	53.31(61)	46.48(68)	38.76(78)	34.44(86)	29.63(96)	24.1(11)	22.29(32)	18.98(37)	17.3(15)	16.14(42)	14.03(47)	11.49(55)	8.38(70)	2.88(88)
Stack ID	A	A	A	A	A	A	B	B	A	B	B	B	B	B
^{43}K (σ_c)	1.55(11)	0.889(67)	0.189(17)	0.0462(42)	–	–	–	–	–	–	–	–	–	–
^{44m}Sc (σ_i)	12.60(72)	12.37(63)	15.20(93)	17.8(11)	16.8(11)	8.63(53)	4.26(24)	1.451(82)	1.317(88)	1.269(95)	0.839(70)	–	–	–
^{44g}Sc (σ_i)	25.0(24)	27.0(22)	37.0(29)	52.6(48)	47.8(39)	29.9(30)	8.09(45)	3.49(20)	2.70(31)	3.02(23)	2.49(21)	–	–	–
^{44g}Sc (σ_c)	37.6(25)	39.4(23)	52.2(31)	70.4(49)	64.7(40)	38.6(31)	12.35(51)	4.94(22)	4.02(32)	4.29(25)	3.33(22)	–	–	–
^{47}Sc (σ_c)	21.2(12)	20.5(10)	21.7(13)	23.5(14)	25.1(16)	15.63(97)	11.53(70)	5.50(32)	2.75(18)	1.57(12)	0.810(67)	0.361(21)	0.218(23)	–
^{48}Sc (σ_i)	1.66(13)	1.68(19)	1.29(15)	0.772(65)	0.700(64)	0.339(26)	0.318(18)	0.185(13)	0.135(14)	0.0625(55)	–	–	–	–

Table 4 Measured isomer-to-ground-state branching ratios for the various ^{nat}Fe(p,x) and ^{nat}Ti(p,x) reaction products observed in this work. Uncertainties are listed in the least significant digit, that is, 0.417(38) means 0.417 ± 0.038. Stack ID specifies which irradiation each measurement belongs to – Stack "A" designates the 55 MeV irradiation, Stack "B" designates the 25 MeV irradiation

	Isomer branching ratio													
E_p (MeV)	53.45(61)	46.63(68)	38.93(78)	34.62(85)	29.84(96)	24.4(11)	22.71(43)	19.36(56)	17.6(15)	16.54(48)	14.52(49)	12.11(53)	9.23(61)	4.10(73)
Stack ID	A	A	A	A	A	A	B	B	A	B	B	B	B	B
^{nat}Fe(p,x)^{52}Mn	0.417(38)	0.414(37)	0.396(40)	0.388(37)	0.517(49)	0.420(40)	0.358(29)	0.202(17)	0.404(56)	0.638(76)	0.92(12)	–	–	–
^{nat}Fe(p,x)^{58}Co	–	–	–	0.326(28)	0.387(34)	0.485(40)	0.583(47)	0.614(49)	0.420(41)	0.486(55)	0.341(40)	0.299(26)	0.234(31)	0.214(39)
E_p (MeV)	53.31(61)	46.48(68)	38.76(78)	34.44(86)	29.63(96)	24.1(11)	22.29(32)	18.98(37)	17.3(15)	16.14(42)	14.03(47)	11.49(55)	8.38(70)	2.88(88)
Stack ID	A	A	A	A	A	A	B	B	A	B	B	B	B	B
^{nat}Ti(p,x)^{44}Sc	0.335(29)	0.314(24)	0.291(25)	0.253(23)	0.260(23)	0.224(23)	0.345(24)	0.294(21)	0.328(34)	0.296(28)	0.252(27)	–	–	–

Table 5 Default settings for the reaction codes

Code version	Proton/neutron optical model	Alpha optical model	E1 γSF model	Level density model
EMPIRE-3.2.3 [47]	Koning-Delaroche [48]	Avrigeanu (2009) [49]	Modified Lorentzian [50]	Enhanced Generalized Superfluid [51].
TALYS-1.8 [52]	Koning-Delaroche	Specific folded potential [52]	Brink-Axel Lorentzian [52]	Gilbert-Cameron [53]
CoH-3.5.3 [54,55]	Koning-Delaroche	Avrigeanu(1994) [56]	Generalized Lorentzian [54,55]	Gilbert-Cameron
ALICE-2017 [57]	Nadasen [58]	Parabolic Diffuse-Well [59]	Berman-Fultz Lorentzian [60]	Kataria-Rarnamurthy-Kapoor [61,62]

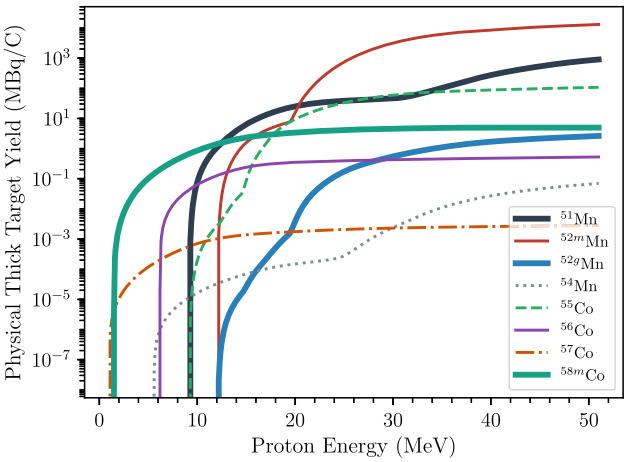

Fig. 3 Integral thick target yields for ^{nat}Fe(p,x)^{51,52m,52g,54}Mn and ^{nat}Fe(p,x)^{55,56,57,58m}Mn, including indirect production routes. Yields are specified in units of MBq/C [63], and represent physical yields (also known as instantaneous production rates). 1 MBq/C= 0.0036 MBq/μAh

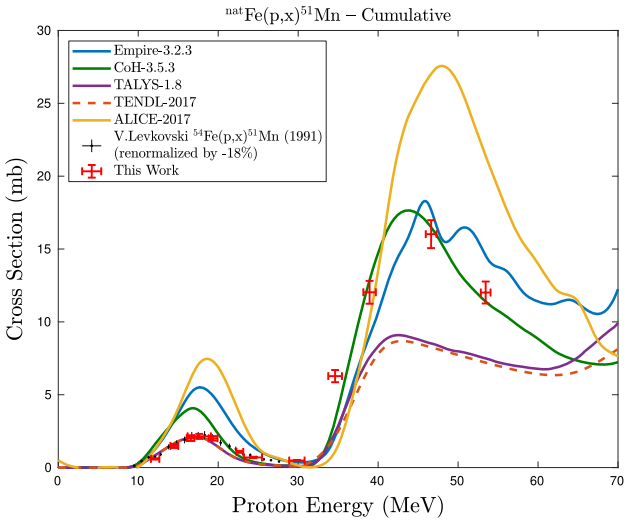

Fig. 4 Measured ^{nat}Fe(p,x)^{51}Mn cross section, with the ^{54}Fe(p,α)^{51}Mn reaction channel visibly peaking at approximately 15 MeV

It should be noted that Fe(p,x)^{51}Mn appears to offer a compelling alternative to the more established ^{50}Cr(d,x)^{51}Mn pathway, which necessitates an enriched ^{50}Cr target to avoid radio-manganese contamination from reactions on stable isotopes of Cr [66]. ^{nat}Fe(p,x)^{51}Mn could be used for production of ^{51}Mn ($\geq$98.8% radioisotopic purity) below 20 MeV using the ^{54}Fe(p,α)^{51}Mn channel. In addition, this low-energy production is accessible using the international network of small medical and research cyclotrons, enabling in-house production of this short-lived ($t_{1/2}$ = 46.2 $\pm$ 0.1 m [9]) radionuclide. To increase yields over ^{nat}Fe(p,x), an enriched ^{54}Fe target could be used to take advantage of the eight-fold increase in reaction cross section for production using 40–50 MeV protons without opening the additional manganese exit channels accessible on a natural target.

3.2 ^{nat}Fe(p,x)^{52m,g}Mn cross sections

This work presents the first measurement of several observables in this energy region including independent cross sections for ^{nat}Fe(p,x)^{52m,g}Mn, the ^{52m}Mn (2^+) / ^{52g}Mn (6^+) isomer branching ratios via ^{nat}Fe(p,x), as well as extending the ^{nat}Fe(p,x)^{52}Mn excitation function down to the lowest energy to date. Cumulative ^{nat}Fe(p,x)^{52g}Mn reaction measurements exist in earlier work, but this work presents the most well-characterized measurement below 70 MeV to date, with cross sections measured at the 6–10% uncertainty level. This work is consistent with the general body of previous cumulative ^{52g}Mn measurements, with the exception of work from Williams, Lagunas-Solar, and Barchuk, all of which have shown discrepancies with prior data in other reaction channels measured here [67–69].

The ^{52m}Mn (2^+) / ^{52g}Mn (6^+) ratio seen in Figure Fig. 5b shows significant deviation from all of the reaction models and the TENDL database near threshold, indicating potential issues with transmission particle transmission coefficients arising from the optical model. Above threshold the values are are all in keeping with the TENDL and default TALYS calculations and differ significantly from both the default CoH and EMPIRE calculations, indicating potential issues with the angular momentum dependence of the level density. For the ^{nat}Fe(p,x)^{52}Mn cross section, seen in Fig. 5a, the peak at lower energy, which is largely attributable to the ^{56}Fe(p,pα) channel, is well-modeled by TALYS and TENDL. However, the production of ^{52}Mn rises much more rapidly than the data would support above 50 MeV, suggesting an overestimation of the ^{56}Fe(p,3p2n) contribution. CoH and EMPIRE, again, overpredict the cross sections at all energies, but seem to have the correct overall energy dependence.

Through measurement of the ^{nat}Fe(p,x)^{52m}Mn independent cross section , the effect of spin distributions in the unresolved discrete states can be studied. The measured data suggest that the independent cross section to the 2^+ isomer should be a large fraction of the cumulative cross section to ^{52}Mn (which has a 6^+ ground state), over 50% at the peak energy. TALYS predictions show approximately 1.5σ agreement with this measurement, but CoH significantly overestimates this ratio at all energies, and EMPIRE overestimates as well in the pre-equilibrium tail, which indicates that the isomer feeding is not well-modeled in these codes.

Fe(p,x) offers an interesting production pathway for ^{52}Mn. Conventional production uses the low-energy ^{nat}Cr/^{52}Cr (p,n)^{52}Mn pathways, which offer high radioisotopic purity (approximately 99.6%) [2,70]. ^{nat}Fe(p,x) offers a nearly threefold increase in production yield, but the lower radioisotopic purity (99.1% for 20–30 MeV, decreasing to 60.8% by

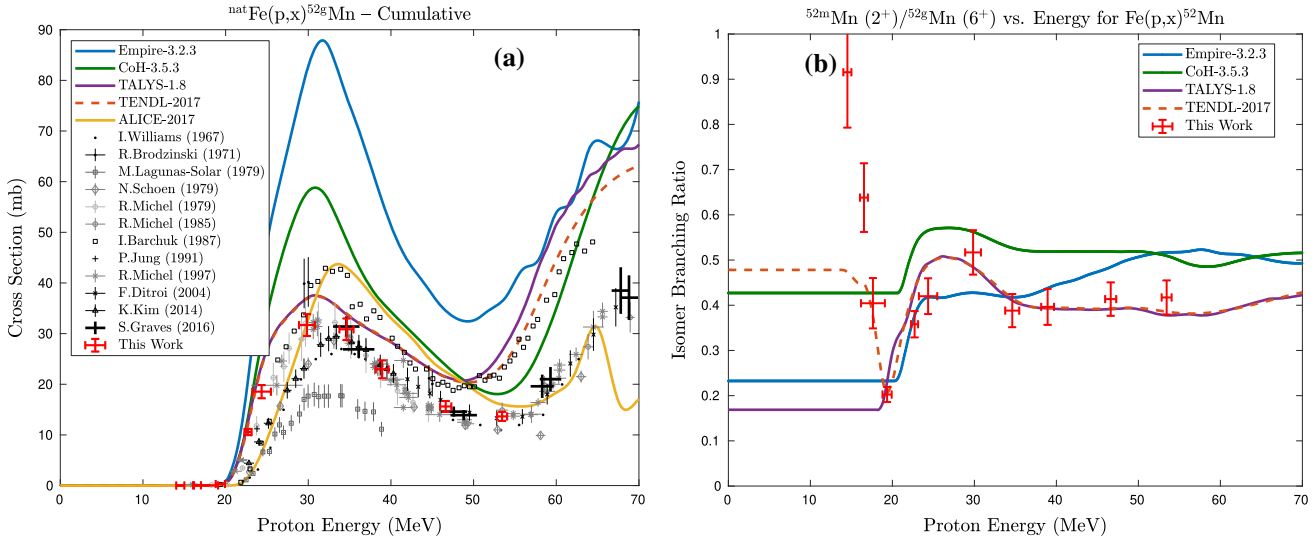

Fig. 5 **a** Measured ^{nat}Fe(p,x)^{52}Mn cross section, with ^{56}Fe(p,αn)^{52}Mn/^{54}Fe(p,2pn)^{52}Mn reaction channels visibly peaking at approximately 30 MeV. **b** Measured ^{52m}Mn (2$^+$) / ^{52g}Mn (6$^+$) isomer branching ratios via ^{nat}Fe(p,x)

40 MeV) at higher energies due to the opening of ^{54}Mn makes this route seem impractical. Much like ^{51}Mn, the use of an enriched ^{54}Fe target would prevent production of ^{54}Mn and long-lived Co radiocontaminants, providing a higher-yield production route over ^{nat}Cr(p,x), with the tradeoff of necessitating higher-energy protons ($\leq$35 MeV) for production. It is important to note that the Fe(p,x) route provides $\geq$60% feeding of ^{52g}Mn ($t_{1/2}$ = 5.591 $\pm$ 0.003 d [8]), implying that the short-lived ^{52m}Mn ($t_{1/2}$ = 21.1 $\pm$ 0.2 m [8]) can be easily separated through the difference in half-life, to avoid the hard 1434 keV gamma-ray produced by the isomer. However, if nearly pure ^{52m}Mn is desired for preclinical imaging applications, the feeding of ^{52}Mn through the ϵ decay of ^{52}Fe ($t_{1/2}$ = 8.725 $\pm$ 0.008 h [8]) exclusively populates the isomer, making this potentially suitable for production through "milking" of a ^{52}Fe generator [71].

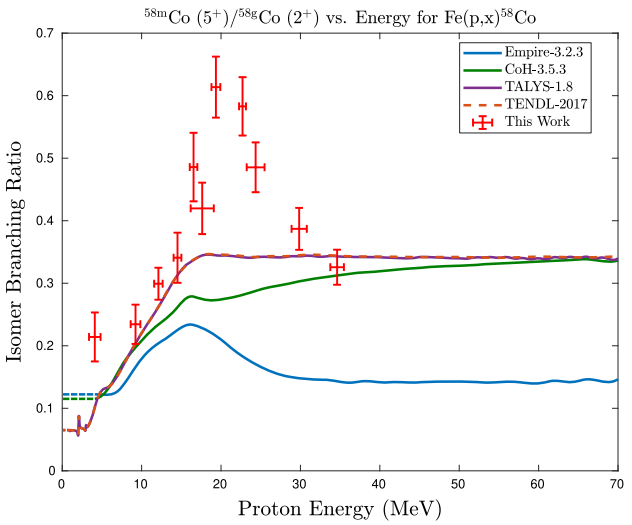

Fig. 6 Measured ^{58m}Co (5$^+$) / ^{58g}Co (2$^+$) isomer branching ratios via ^{nat}Fe(p,x), with the ^{58}Fe(p,n)^{58m}Co reaction channel visibly peaking at approximately 20 MeV

3.3 ^{nat}Fe(p,x)^{56,58}Co cross sections

This work presents the first measurements of several observables in this energy region, including the ^{nat}Fe(p,x)^{58m}Co reactions in the 0–70 MeV region, the independent cross sections for ^{nat}Fe(p,x)^{58g}Co, and the ^{58m}Co (5$^+$) / ^{58g}Co (2$^+$) isomer branching ratios via ^{nat}Fe(p,x), seen in Fig. 6. The cumulative cross sections from these data are both consistent with, and higher-precision than, existing measurements of the cumulative ^{nat}Fe(p,x)^{58g}Co cross sections, as well as the large body of measurements for ^{nat}Fe(p,x)^{56}Co.

While it is dangerous to use weak channels to guide reaction modeling, EMPIRE and TALYS/TENDL all reproduce earlier work and this measurement reasonably well ($\pm$10%) for the ^{nat}Fe(p,x)^{58g}Co reaction channel, as well as the strongly-fed ^{nat}Fe(p,x)^{56}Co reaction. This holds for both the shape and magnitude of each excitation function. CoH overestimates the ^{nat}Fe(p,x)^{58g}Co peak magnitude by approximately 30% and ^{nat}Fe(p,x)^{56}Co by approximately 10%, despite matching the rising and falling edges of the curve. For both the ^{nat}Fe(p,x)^{56,58g}Co channels, ALICE underestimates the magnitude of the rising edge and compound peak by nearly 50%, though it shows the best agreement of these codes with the magnitude of the pre-equilibrium tails for these channels.

However, all codes fail to reproduce the magnitude of the ^{nat}Fe(p,x)^{58m}Co peak by approximately 25% and completely

fail to reproduce the pre-equilibrium tail for this channel, as measured in this work. As opposed to the other isomer-to-ground state ratio measured for Fe, the opposite is seen for ^{nat}Fe(p,x)^{58}Co – the codes underpredict the ratio of the isomer-to-ground state, but in this case the isomer is the higher spin state (5^+, compared with a 2^+ ground state). Given that the level density model was the same for all of the product nuclei, it points to issues in the spin distribution of the initial population of the residual nucleus in the pre-equilibrium neutron emission.

The ^{nat}Fe(p,x)^{56}Co channel ($t_{1/2}$ = 77.236 ± 0.026 d, ϵ=100% to ^{56}Fe [29]) could be useful as an experimental monitor reaction due to its high intensity and production of long-lived residual products that produce bright decay gamma-rays. Given that ^{nat}Cu(p,x)^{56}Co is an established monitor reaction, it seems likely that an evaluation of ^{nat}Fe(p,x)^{56}Co as a monitor standard could provide a useful complement to existing low-to-intermediate energy monitor reactions. A similar argument can also be applied to ^{nat}Fe(p,x)^{58}Co, which is another established copper monitor reaction product. While this channel shares many of the same attractive features as ^{nat}Fe(p,x)^{56}Co, the weak feeding of ^{58}Co makes this far less of an attractive option in comparison.

In addition to the ^{nat}Fe(p,x)^{51,52}Mn measurements, this experiment has also yielded production cross section measurements of a number of additional emerging radionuclides with medical applications, including the non-standard positron emitter ^{55}Co [72–74]. Production of this radionuclide offers no major advantages over established pathways, with the lower yield and radioisotopic purity failing to justify the convenience of natural targets via ^{nat}Fe(p,x). The one potential exception to this is the production of ^{58m}Co, a potent agent for Auger electron-based targeted therapy [75–77]. While ingrowth of the long-lived ^{58g}Co ($t_{1/2}$ = 70.86(6) d [31]) is unavoidable, lowering the co-production of ^{58g}Co is necessary to minimize patient dose. The ^{nat}Fe(p,x)^{58m}Co pathway shows a clear "peak" in the ^{58m}Co/^{58g}Co branching ratio for approximately 15–30 MeV protons, which might have translational implications if Auger electron therapy becomes more clinically prevalent.

3.4 ^{nat}Fe(p,x)^{49,51}Cr cross sections

This work presents the first measurement of ^{nat}Fe(p,x)^{49}Cr and the first independent cross sections for ^{nat}Fe(p,x)^{51}Cr in this energy region, seen in Fig. 7. The cumulative cross sections from these data are also consistent with existing measurements of the cumulative ^{nat}Fe(p,x)^{51}Cr cross sections, and with improved precision. As seen in other channels, the work of Williams and Schoen [69,78] are both significantly lower in magnitude, and with cross sections peaking approximately 5 MeV higher than body of other measurements. While the ^{51}Cr decay data used in these experiments (Williams: $t_{1/2}$ = 27.8 d, I_γ=9%, Schoen: $t_{1/2}$ = 27.71 d, I_γ=10.2%) differ slightly from those used here ($t_{1/2}$ = 27.704(3) d, I_γ=9.910(10)% [9]), these differences do not account for the approximately 50% smaller peak cross section reported by Williams, and 30% smaller for Schoen. Neither publication reports any discussion of this channel, nor do they detail the length of each irradiation, suggesting that transient equilibrium from the ^{51}Mn decay precursor was either not considered, or mis-calculated [79].

For both the ^{49,51}Cr channels, the shape is well-modeled by all codes in the energy range covered in this measurement, though ALICE appears to peak approximately 3 MeV higher than the other codes. For ^{49}Cr, ALICE and CoH both overestimate the magnitude of this channel by approximately 30%, ALICE overestimates by approximately 350%, while TALYS and TENDL underestimate the magnitude by approximately 50%. However, it should be noted that weakly-produced nuclides should not be used to guide reaction modeling due to their sensitivity to stronger reaction channels. Modeling of ^{51}Cr shows improved agreement in magnitude – CoH and ALICE are consistent at the 1σ level, EMPIRE overestimates the peak by approximately 25%, and TALYS/TENDL underestimate the peak by approximately 60%. However, this level of disagreement is more concerning than for ^{49}Cr, due to the strong feeding of this channel. This observation provides a clear illustration that both TALYS/TENDL tend to either match or significantly underestimate, but never overestimate, the magnitude of many reaction channels below 70 MeV seen in this work. Since the sum of all channel cross sections are constrained by the total reaction cross section, this would suggest that TALYS is either overestimating the feeding of channels with stable residual nuclei, or the elastic/inelastic channels.

3.5 ^{nat}Fe(p,x)^{54,56}Mn cross sections

This work presents the first measurements of the ^{nat}Fe(p,x)^{56}Mn reaction below 70 MeV. Additionally, we report the highest precision measurement of ^{nat}Fe(p,x)^{54}Mn in this energy region. This measurement is consistent with earlier work aside from the globally-discrepant Williams data, as discussed previously. Modeling of these channels presents a counterpoint to the ^{51,52}Mn results discussed earlier — ^{54}Mn is well-modeled by CoH, TENDL, and TALYS, though EMPIRE overestimates the peak cross section by approximately 25%, and ALICE underestimates by the same, in addition to peaking approximately 3 MeV higher. The weakly-fed ^{56}Mn is poorly modeled in comparison, with CoH, EMPIRE, and ALICE failing to match neither the shape nor magnitude of the excitation function, though TALYS/TENDL matches both. While the poorly-modeled ^{51,52}Mn channels are dominated by alpha particle emission, ^{54}Mn production is more

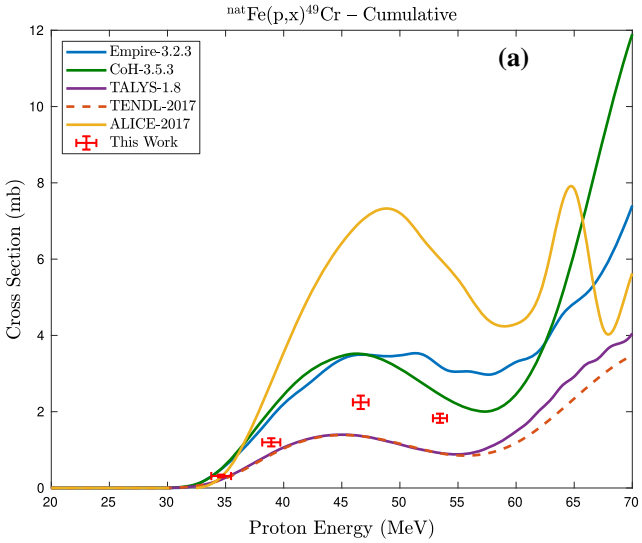

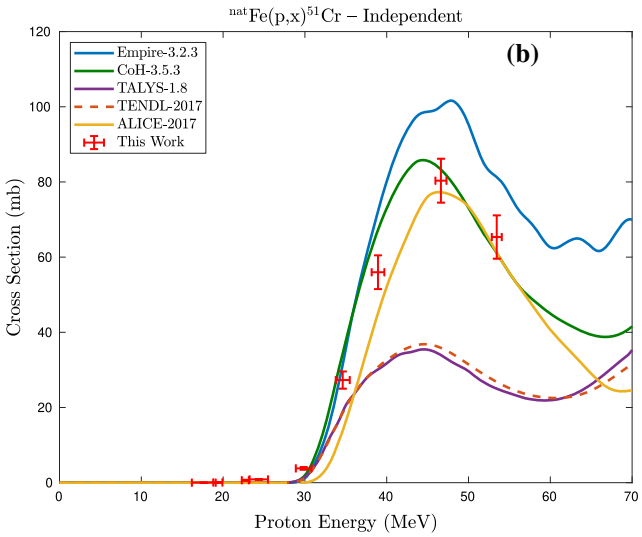

Fig. 7 **a** Measured ^{nat}Fe(p,x)^{49}Cr independent cross section, with the ^{56}Fe(p,αp3n)^{49}Cr/^{54}Fe(p,3p3n)^{49}Cr reaction channels visibly peaking at approximately 48 MeV. **b** Measured ^{nat}Fe(p,x)^{51}Cr independent cross section, with the ^{56}Fe(p,αpn)^{51}Cr/^{54}Fe(p,3pn)^{51}Cr reaction channels visibly peaking at approximately 45 MeV

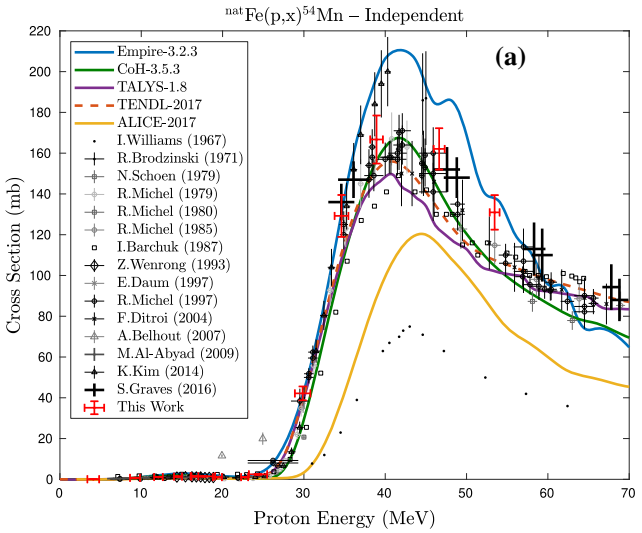

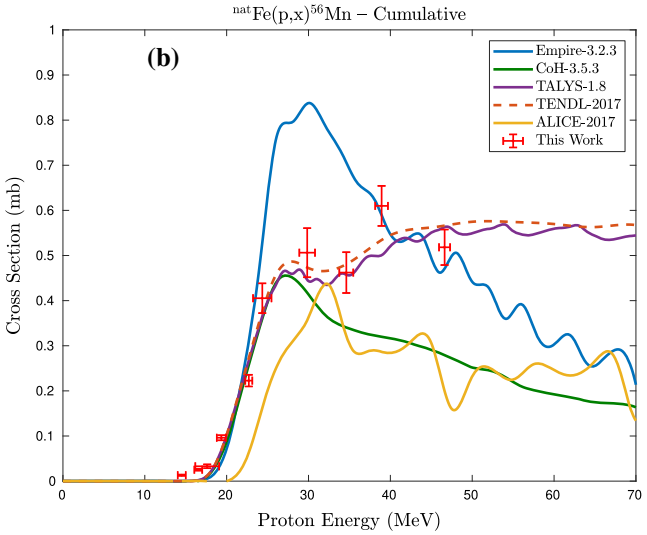

Fig. 8 **a** Measured ^{nat}Fe(p,x)^{54}Mn independent cross section, with the sum of the ^{56}Fe(p,2pn)^{54}Mn and ^{57}Fe(p,2p2n)^{54}Mn reaction channels visibly peaking at approximately 40 MeV. **b** Measured ^{nat}Fe(p,x)^{56}Mn independent cross section, with the ^{57}Fe(p,2p)^{56}Mn/^{58}Fe(p,2pn)^{56}Mn reaction channels visibly peaking at approximately 30 MeV and 40 MeV, respectively

characterized by the the emission of the constituent protons and neutrons. Since TALYS, TENDL, and CoH exhibited poor predictive power for ^{51,52}Mn, but reproduced ^{54}Mn well, this observation would suggest that the alpha optical models employed in these codes are underestimating the strength of alpha emission in this energy region.

Similarly to ^{56}Co, ^{nat}Fe(p,x)^{54}Mn offers another interesting possibility as a ^{nat}Fe(p,x) monitor reaction, with a long half-life ($t_{1/2} = 312.20 \pm 0.020$ d, $\epsilon =$ 100% to ^{54}Cr [27]), strong cross section (approximately 160 mb near 40 MeV), and a uniquely-produced daughter nuclide. This reaction could be useful for intermediate- to high-energy protons ($E_p \geq$30 MeV), but would be susceptible to production via high-energy secondary neutrons (threshold 12.1 MeV off of ^{56}Fe). Additionally, the ^{nat}Fe(p,x)^{54}Mn and ^{nat}Fe(p,x)^{56}Co channels have a difference in apparent energetic thresholds, providing some energy discrimination sensitivity in the same iron foil, particularly in the 20–50 MeV region.

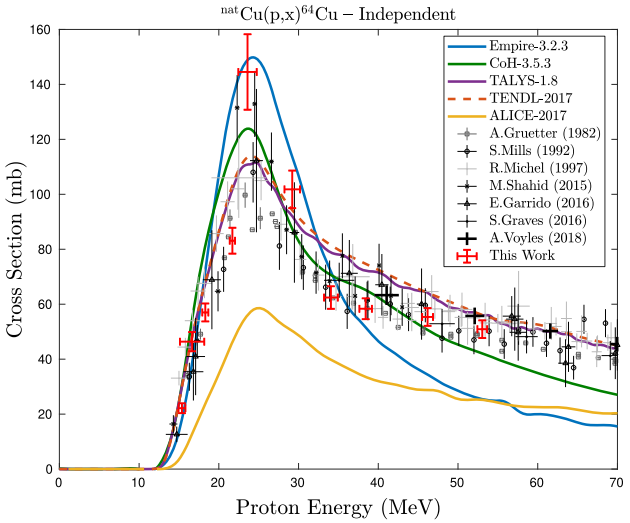

Fig. 9 Measured ^{nat}Cu(p,x)^{64}Cu independent cross section, with the ^{65}Cu(p,pn)^{64}Cu reaction channels visibly peaking at approximately 25 MeV

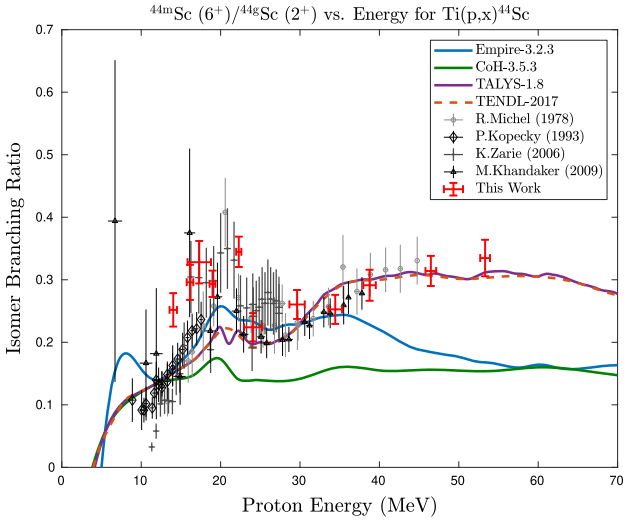

Fig. 10 Measured ^{44m}Sc (6$^+$) / ^{44g}Sc (2$^+$) isomer branching ratios via ^{nat}Ti(p,x)

3.6 ^{nat}Cu(p,x)^{60,61,64}Cu cross sections

As with many ^{nat}Cu(p,x) channels, these reactions have been previously measured in our earlier work, but this measurement extends these cross sections down to reaction thresholds and reports cross sections for many of the short-lived products unable to be observed previously, such as ^{60}Cu [16]. For ^{nat}Cu(p,x)^{60,61,64}Cu, the measurements presented here are consistent with earlier work (aside from that of Williams [69], as discussed earlier), and are generally the highest-precision measurements to date. As part of this work, a discrepancy, outside reported uncertainties, has been observed between the accepted and measured values of the intensity ratio of the 283 keV and 656 keV decay lines in ^{61}Cu, and is detailed in a separate manuscript [80].

As we reported previously, modeling of ^{nat}Cu(p,x) reactions is poor in this energy region. For ^{60}Cu, all codes fail to predict the magnitude and shape of the channel, with a peak approximately 5 MeV lower than observed. Similar behavior is observed in the strongly-fed ^{61}Cu, with the peak shifted approximately 3 MeV lower. ^{64}Cu modeling appears to be the best of these channels, with all codes matching the overall shape, but only EMPIRE predicting the rapid rise and fall of the compound peak. Unlike ALICE and EMPIRE, CoH, TALYS, and TENDL all do a successful job of modeling the shape of the (p,pn) pre-equilibrium tail, with this channel showing the best predictive power of the ^{nat}Cu(p,x) reactions. As seen with ALICE for ^{61}Cu/^{64}Cu, the alternating underestimation/overestimation across channels for a single code points to competition between neighboring reaction channels as a common issue in this mass region.

^{nat}Cu(p,x) also yielded measurements of a number of additional medical radionuclides, including the non-standard positron emitters ^{57}Ni [7,81–83], ^{61}Cu [84,85], and ^{64}Cu [86–93]. However, production of these radionuclides offers no major advantages over established pathways, with the lower yield and radioisotopic purity failing to justify the convenience of natural targets via ^{nat}Cu(p,x).

3.7 ^{nat}Ti(p,x)^{44,47,48}Sc cross sections

While the focus of this work is on the production of ^{51,52}Mn and other ^{nat}Fe(p,x) channels, the cross sections reported here offer improvements to prior work, particularly for the several Sc radionuclides observed. For all of the ^{nat}Ti(p,x)^{44,47,48}Sc channels, this work is consistent with all prior data and is generally the highest-precision measurement to date. This work additionally extends the ^{44g}Sc excitation function to the highest energy to date.

The modeling of these channels is markedly improved in comparison to the ^{nat}Fe(p,x) channels discussed previously. For ^{44m}Sc, all codes place the compound peak approximately 4 MeV lower than observed, and EMPIRE overestimates the magnitude of this peak, while TALYS, TENDL, and CoH significantly underestimate it. Notably, the pre-equilibrium tail and transition towards a second peak near 65 MeV is well-modeled by TALYS/TENDL, but significantly underestimated by EMPIRE and CoH. The same modeling trend is observed for ^{44m}Sc, and reflected in the measured isomer branching ratios for ^{44}Sc, seen in Fig. 10. Above 23 MeV, TALYS/TENDL both reproduce the present work, as well as earlier measurements, suggesting that angular momentum transfer in the pre-equilibrium regime is being well-modeled, but that the total feeding of the ^{44}Sc channel is underesti-

mated. A similar argument holds for EMPIRE, which reproduces the isomer branching up to 35 MeV. However, CoH fails to reproduce either the channel magnitude or the isomer ratio. ^{47}Sc presents a very opposed situation, despite an abundance of reaction data and strong feeding of the channel. All codes fail to reproduce either the shape or magnitude of this channel, with only CoH able to predict the compound peak but unble to model the pre-equilibrium tail. As a cumulative reaction channel, it is unclear whether this failure arises from modeling of any ^{47}Ca decay precursors, or the competition between ^{48}Ti(p,20)^{47}Sc / ^{49}Ti(p,2pn)^{47}Sc / ^{50}Ti(p,α)^{47}Sc channels. Modeling of ^{48}Sc is lacking, with only TALYS/TENDL matching the shape of the excitation, and all codes failing to reproduce the magnitude of the channel.

As with ^{58m}Co measurements, the titanium activation has yielded measurements of a number of additional medical radionuclides, including the non-standard positron emitter ^{44}Sc [94–96] and the β^--therapeutic agent ^{47}Sc [97,98]. However, this route offers no major advantages over established ^{44}Ca(p,n) / ^{44}Ca(d,2n) / ^{45}Sc(p,2n)^{44}Ti $\xrightarrow{\epsilon}$ ^{44}Sc pathways. Since high-specific activity ^{47}Sc production routes are limited (with ^{47}Ti(n,p)^{47}Sc as one of few potential candidates), alternative pathways are greatly desired by the community. However, ^{nat}Ti(p,x) is clearly not a compelling alternative if high specific activity is required, due to the inability to avoid co-production of long-lived Sc radiocontaminants.

4 Conclusions

We present here a set of measurements of 34 cross sections for the ^{nat}Fe(p,x), ^{nat}Cu(p,x), and ^{nat}Ti(p,x) reactions up to 55 MeV, as well as independent measurements of three isomer branching ratios. Nearly all cross sections have been reported with higher precision than previous measurements. We report the first measurements for $\leq$70 MeV protons of the ^{nat}Fe(p,x)^{49}Cr, ^{nat}Fe(p,x)^{51}Mn, ^{nat}Fe(p,x)^{52m}Mn, ^{nat}Fe(p,x)^{56}Mn, and ^{nat}Fe(p,x)^{58m}Co reactions, as well as the first measurement of the independent cross sections for ^{nat}Fe(p,x)^{51}Cr, ^{nat}Fe(p,x)^{52g}Mn, ^{nat}Fe(p,x)^{58g}Co, and the ^{52m}Mn (2^+) / ^{52g}Mn (6^+) and ^{58m}Co (5^+) / ^{58g}Co (2^+) isomer branching ratios via ^{nat}Fe(p,x). Clearly, the use of Fe(p,x)^{51,52}Mn has significant untapped potential, and additional work is needed to further characterize these reaction channels for E_p $\leq$60 MeV, as well as the potential for ^{nat}Fe(p,x)^{54}Mn,^{56}Co as future monitor reactions.

We also use these measurements to illustrate the deficiencies in the current state of reaction modeling up to 55 MeV for ^{nat}Fe(p,x), ^{nat}Cu(p,x), and ^{nat}Ti(p,x) reactions. Across the channels studied here, there exists a clear trend of modeling codes failing to reproduce observed reaction thresholds, suggesting an underlying problem with the transmission coefficients utilized in these models. While no model globally succeeds in these channels, TALYS and TENDL generally perform best with the lower-energy "compound" reactions but, like all models, do not accurately predict the higher-energy reactions that have a significant pre-equilibrium component. This illustrates the importance of a well-characterized level density model for predictive power, as the "simple" Gilbert-Cameron model, lacking an energy-dependent spin parameter, outperforms in the modeling of the pre-equilibrium regime.

It is important to note that overall, modeling succeeds best where experimental data exist, underpinning the need for measurement of all observed reaction channels in experiments. This work offers a clear warning against unchecked use of such default calculations, even if performed with the latest developments in nuclear reaction modeling codes. For work requiring even modest accuracy (say 20%) in their default predictive capabilities, these codes clearly cannot be used to satisfaction. Finally, this work provides another example of the current issues with modeling of stopping power in stacked target charged particle irradiation experiments, corrected using variance minimization techniques.

Acknowledgements The authors would like to particularly acknowledge the assistance and support of Brien Ninemire, Scott Small, Tom Gimpel, and all the rest of the operations, research, and facilities staff of the LBNL 88-Inch Cyclotron. We also wish to acknowledge Alexander Springer and Haleema Zaneb, who participated in these experiments. This research is supported by the U.S. Department of Energy Isotope Program, managed by the Office of Science for Nuclear Physics. This work has been carried out under the auspices of the U.S. Department of Energy by Lawrence Berkeley National Laboratory and the U.S. Nuclear Data Program under contract # DE-AC02-05CH11231. This research was performed under appointment to the Rickover Fellowship Program in Nuclear Engineering, sponsored by the Naval Reactors Division of the U.S. Department of Energy. Additional support has been provided by the U.S. Nuclear Regulatory Commission.
This research used the Savio computational cluster resource provided by the Berkeley Research Computing program at the University of California, Berkeley (supported by the UC Berkeley Chancellor, Vice Chancellor for Research, and Chief Information Officer).

Data Availability Statement The gamma-ray spectra and all other raw data created during this research are openly available at: https://doi.org/10.5281/zenodo.3596977 [99]. All other derived data are available from the corresponding author on reasonable request. See Supplemental Material at https://doi.org/10.1140/epja/s10050-021-00401-2 for a tabulation of the relevant nuclear data used in the analysis for the present work.

Appendix A: Stack design

See Table 6.

Table 6 Specifications of the 25 MeV and 55 MeV target stack designs in the present work. The proton beam enters the stack upstream of the SS-5 and SS-3 profile monitors, respectively, and travels through the stack in the order presented here. The 6061 aluminum degraders have a measured density of approximately 2.68 ± 0.03 g/cm^3. Their areal densities were determined using the variance minimization techniques described in this work and an earlier paper [16]. A 316 stainless steel foil is inserted at both the front and rear of each target stack as a monitor of the beam's spatial profile by developing radiochromic film (Gafchromic EBT3) after end-of-bombardment. All Fe/Ti/Cu activation foils were each covered on both sides by 3M 5413-Series Kapton polyimide film tape, each piece of tape consisting of 43.2 μm of a silicone adhesive (nominal 4.79 mg/cm^2) on 25.4 μm of a polyimide backing (nominal 3.61 mg/cm^2). Similarly to the aluminum degraders, the effective areal density of the Kapton tape was determined through variance minimization, suggesting an effective 5.69% enhancement of the nominal values

25 MeV Target layer	Measured thickness	Measured areal density (mg/cm^2)	55 MeV Target layer	Measured thickness	Measured areal density (mg/cm^2)
SS profile monitor SS-5	130.94 μm	100.57 ± 0.17%	SS profile monitor SS-3	130.9 μm	100.48 ± 0.17%
Fe-08	26.25 μm	19.69 ± 0.17%	Fe-01	25.75 μm	20.22 ± 0.21%
Ti-14	25.01 μm	10.87 ± 0.36%	Ti-01	25.88 μm	11.09 ± 0.16%
Cu-14	24.01 μm	17.49 ± 0.40%	Cu-01	28.81 μm	22.40 ± 0.11%
Al Degrader E-09	256.5 μm	–	Al Degrader A-1	2.24 mm	–
Fe-09	26.5 μm	19.90 ± 0.09%	Fe-02	25.5 μm	19.91 ± 0.13%
Ti-15	23.81 μm	10.97 ± 0.11%	Ti-02	25.74 μm	10.94 ± 0.24%
Cu-15	21.81 μm	17.63 ± 0.46%	Cu-02	28.75 μm	22.32 ± 0.40%
Al Degrader H-01	127.09 μm	–	Al Degrader A-2	2.24 mm	–
Fe-10	26.5 μm	19.84 ± 0.11%	Fe-03	25.25 μm	20.00 ± 0.27%
Ti-16	24.6 μm	10.96 ± 0.32%	Ti-03	25.91 μm	11.25 ± 0.15%
Cu-16	22.01 μm	17.22 ± 0.25%	Cu-03	28.86 μm	22.49 ± 0.20%
Fe-11	27.26 μm	19.96 ± 0.17%	Al Degrader C-1	0.97 mm	–
Ti-17	25.01 μm	10.88 ± 0.25%	Fe-04	25.25 μm	19.93 ± 0.33%
Cu-17	28.82 μm	21.91 ± 0.33%	Ti-04	25.84 μm	10.91 ± 0.18%
Fe-12	27.01 μm	20.03 ± 0.12%	Cu-04	28.78 μm	22.38 ± 0.29%
Ti-18	25.01 μm	11.00 ± 0.87%	Al Degrader C-2	0.97 mm	–
Cu-18	28.75 μm	22.33 ± 0.14%	Fe-05	25.64 μm	20.02 ± 0.24%
Fe-13	26.25 μm	20.05 ± 0.16%	Ti-05	25.86 μm	10.99 ± 0.30%
Ti-19	26.6 μm	11.01 ± 0.22%	Cu-05	28.77 μm	22.35 ± 0.12%
Cu-19	28.79 μm	22.32 ± 0.19%	Al Degrader C-3	0.97 mm	–
Fe-14	25.75 μm	20.11 ± 0.19%	Fe-06	25.75 μm	20.21 ± 0.26%
Ti-20	27.01 μm	11.06 ± 0.35%	Ti-06	25.5 μm	11.15 ± 0.23%
Cu-20	28.26 μm	22.34 ± 0.28%	Cu-06	28.83 μm	22.43 ± 0.10%
SS profile monitor SS-6	131.5 μm	100.99 ± 0.17%	Al Degrader C-4	0.97 mm	–
			Fe-07	25.76 μm	19.93 ± 0.19%
			Ti-07	25.75 μm	11.17 ± 0.33%
			Cu-07	28.76 μm	22.34 ± 0.24%
			SS profile monitor SS-4	131.21 μm	101.25 ± 0.16%

Appendix B: Measured excitation functions

Figures of the cross sections measured in this work are presented here, in comparison with literature data [7,16,65,67–69,78,100–129].

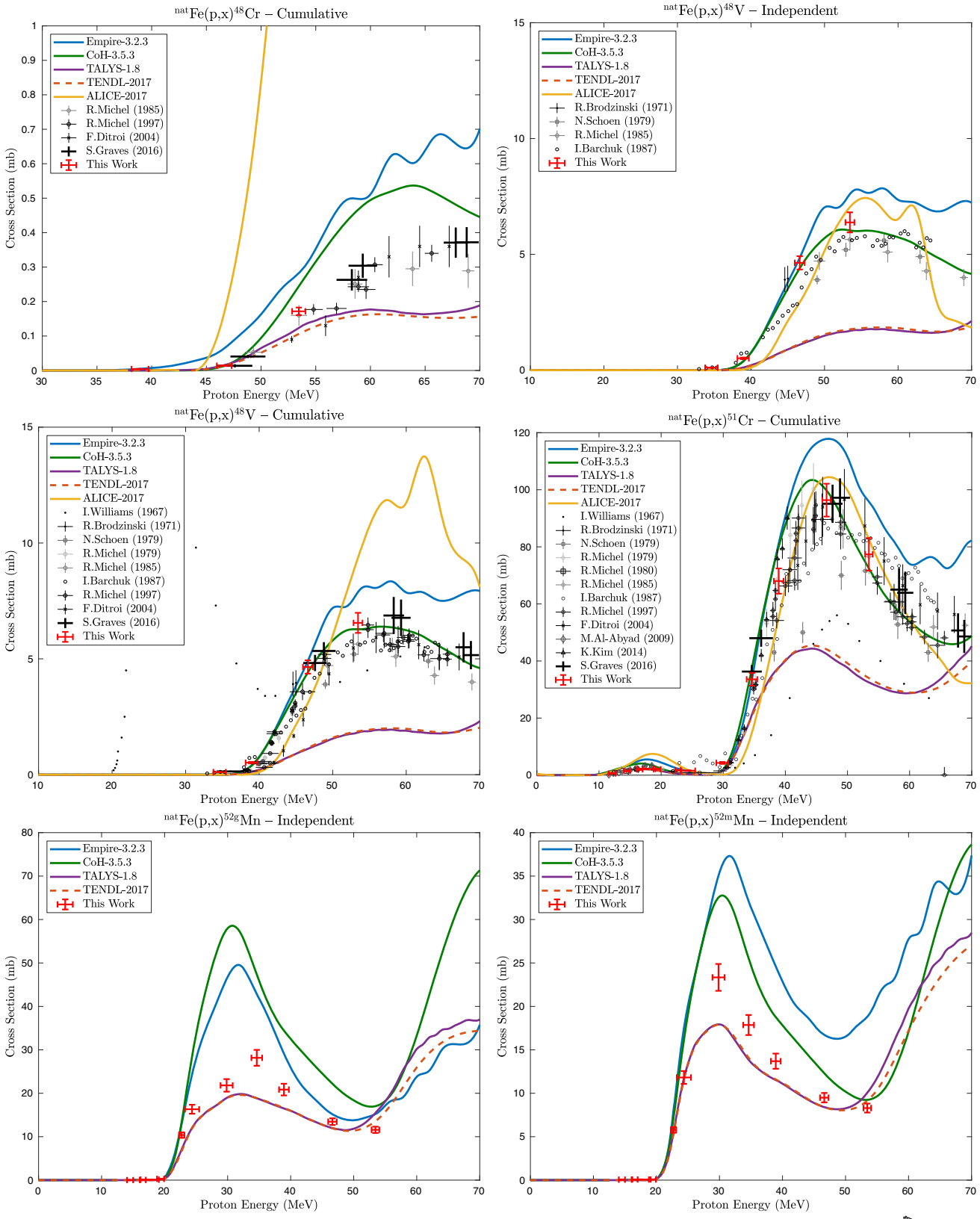

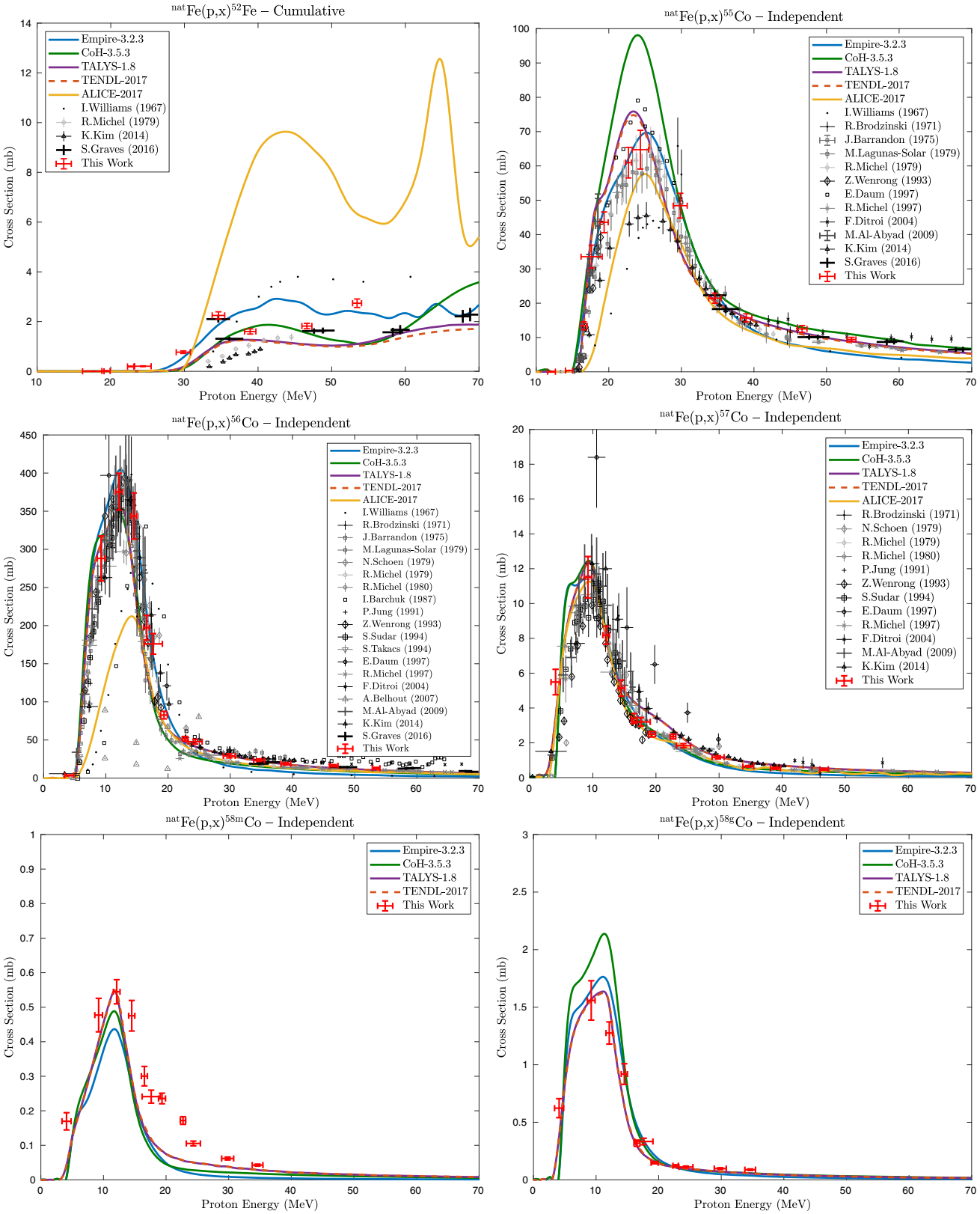
natFe(p,x)52Fe – Cumulative
Empire-3.2.3
CoH-3.5.3
TALYS-1.8
TENDL-2017
ALICE-2017
I.Williams (1967)
R.Michel (1979)
K.Kim (2014)
S.Graves (2016)
This Work
Cross Section (mb)
Proton Energy (MeV)
natFe(p,x)55Co – Independent
Empire-3.2.3
CoH-3.5.3
TALYS-1.8
TENDL-2017
ALICE-2017
I.Williams (1967)
R.Brodzinski (1971)
J.Barrandon (1975)
M.Lagunas-Solar (1979)
R.Michel (1979)
Z.Wenrong (1993)
E.Daum (1997)
R.Michel (1997)
F.Ditroi (2004)
M.Al-Abyad (2009)
K.Kim (2014)
S.Graves (2016)
This Work
Cross Section (mb)
Proton Energy (MeV)
natFe(p,x)56Co – Independent
Empire-3.2.3
CoH-3.5.3
TALYS-1.8
TENDL-2017
ALICE-2017
I.Williams (1967)
R.Brodzinski (1971)
J.Barrandon (1975)
M.Lagunas-Solar (1979)
N.Schoen (1979)
R.Michel (1979)
R.Michel (1980)
I.Barchuk (1987)
P.Jung (1991)
Z.Wenrong (1993)
S.Sudar (1994)
S.Takacs (1994)
E.Daum (1997)
R.Michel (1997)
F.Ditroi (2004)
A.Belhout (2007)
M.Al-Abyad (2009)
K.Kim (2014)
S.Graves (2016)
This Work
Cross Section (mb)
Proton Energy (MeV)
natFe(p,x)57Co – Independent
Empire-3.2.3
CoH-3.5.3
TALYS-1.8
TENDL-2017
ALICE-2017
R.Brodzinski (1971)
N.Schoen (1979)
R.Michel (1979)
R.Michel (1980)
P.Jung (1991)
Z.Wenrong (1993)
S.Sudar (1994)
E.Daum (1997)
R.Michel (1997)
F.Ditroi (2004)
M.Al-Abyad (2009)
K.Kim (2014)
This Work
Cross Section (mb)
Proton Energy (MeV)
natFe(p,x)58mCo – Independent
Empire-3.2.3
CoH-3.5.3
TALYS-1.8
TENDL-2017
This Work
Cross Section (mb)
Proton Energy (MeV)
natFe(p,x)58gCo – Independent
Empire-3.2.3
CoH-3.5.3
TALYS-1.8
TENDL-2017
This Work
Cross Section (mb)
Proton Energy (MeV)

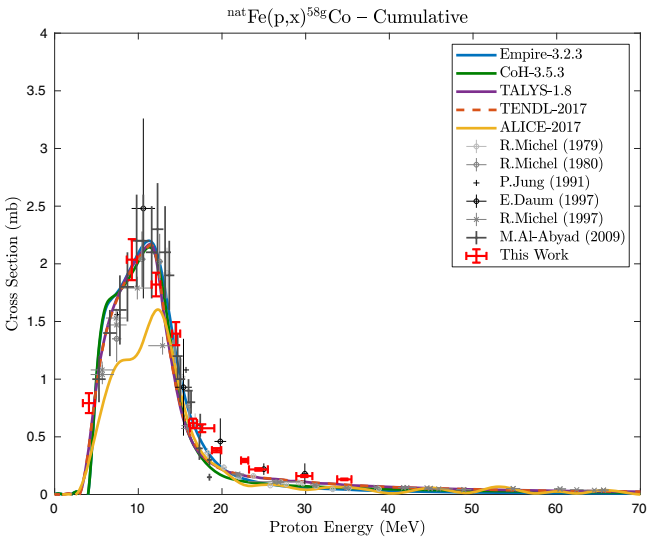
^{nat}Fe(p,x)^{58g}Co – Cumulative
Empire-3.2.3
CoH-3.5.3
TALYS-1.8
TENDL-2017
ALICE-2017
R.Michel (1979)
R.Michel (1980)
P.Jung (1991)
E.Daum (1997)
R.Michel (1997)
M.Al-Abyad (2009)
This Work
Cross Section (mb)
Proton Energy (MeV)

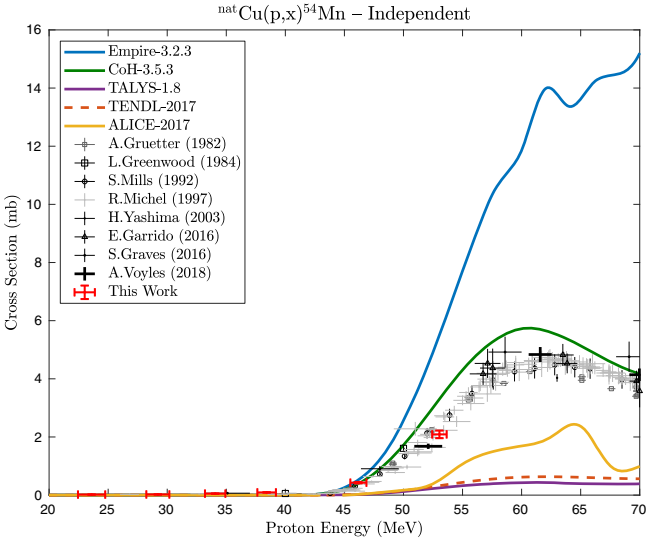
^{nat}Cu(p,x)^{54}Mn – Independent
Empire-3.2.3
CoH-3.5.3
TALYS-1.8
TENDL-2017
ALICE-2017
A.Gruetter (1982)
L.Greenwood (1984)
S.Mills (1992)
R.Michel (1997)
H.Yashima (2003)
E.Garrido (2016)
S.Graves (2016)
A.Voyles (2018)
This Work
Cross Section (mb)
Proton Energy (MeV)

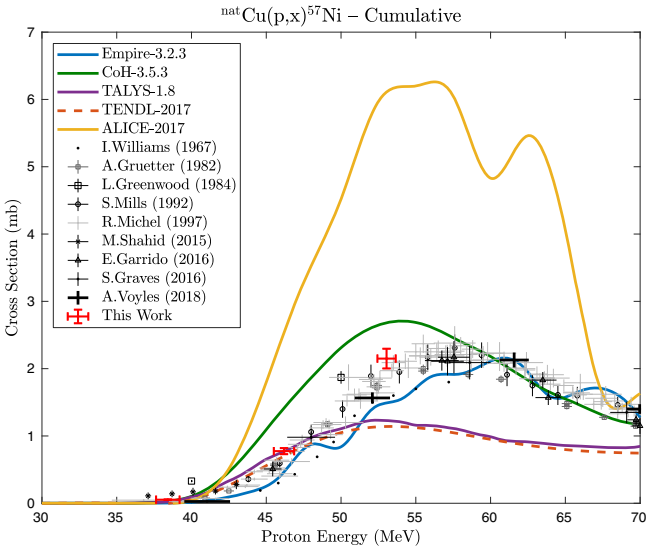
^{nat}Cu(p,x)^{57}Ni – Cumulative
Empire-3.2.3
CoH-3.5.3
TALYS-1.8
TENDL-2017
ALICE-2017
I.Williams (1967)
A.Gruetter (1982)
L.Greenwood (1984)
S.Mills (1992)
R.Michel (1997)
M.Shahid (2015)
E.Garrido (2016)
S.Graves (2016)
A.Voyles (2018)
This Work
Cross Section (mb)
Proton Energy (MeV)

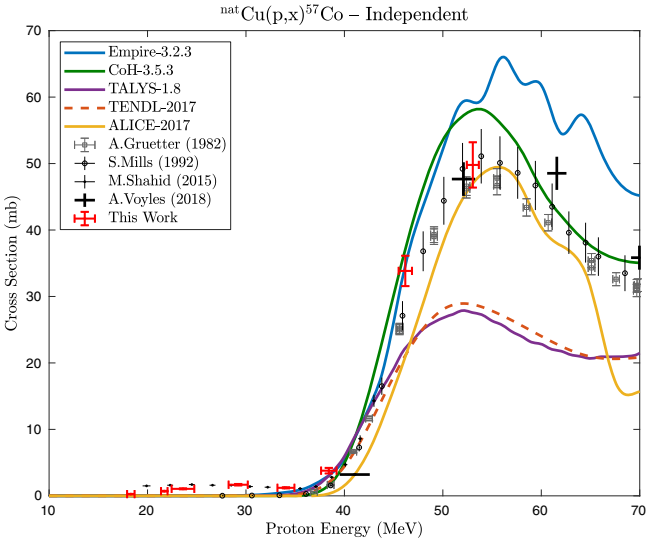
^{nat}Cu(p,x)^{57}Co – Independent
Empire-3.2.3
CoH-3.5.3
TALYS-1.8
TENDL-2017
ALICE-2017
A.Gruetter (1982)
S.Mills (1992)
M.Shahid (2015)
A.Voyles (2018)
This Work
Cross Section (mb)
Proton Energy (MeV)

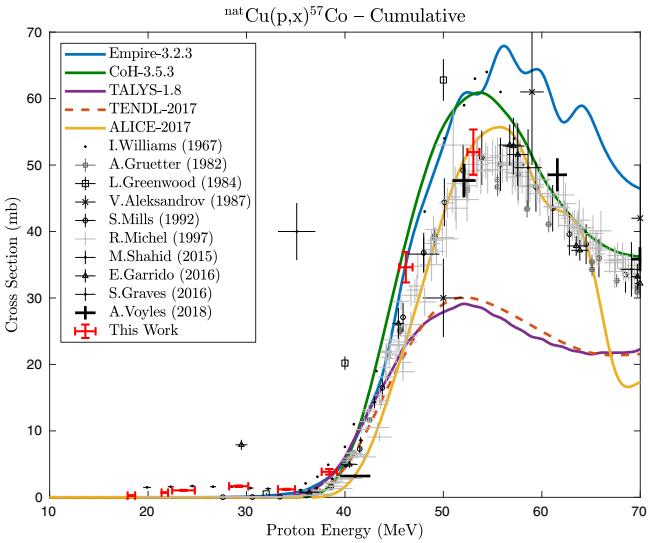
^{nat}Cu(p,x)^{57}Co – Cumulative
Empire-3.2.3
CoH-3.5.3
TALYS-1.8
TENDL-2017
ALICE-2017
I.Williams (1967)
A.Gruetter (1982)
L.Greenwood (1984)
V.Aleksandrov (1987)
S.Mills (1992)
R.Michel (1997)
M.Shahid (2015)
E.Garrido (2016)
S.Graves (2016)
A.Voyles (2018)
This Work
Cross Section (mb)
Proton Energy (MeV)

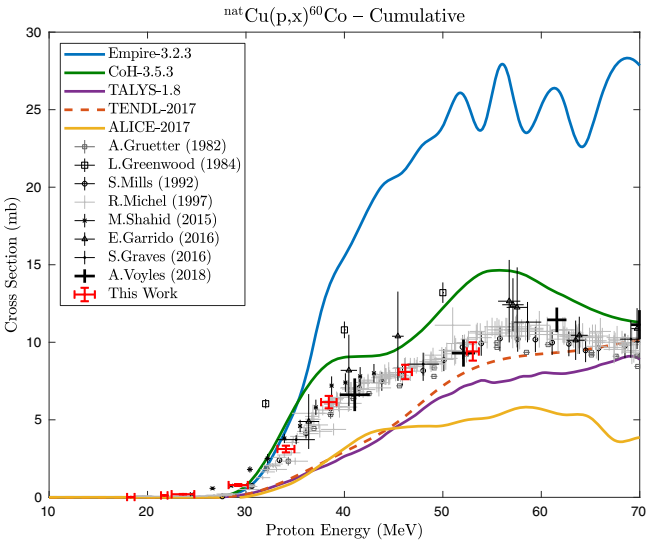
^{nat}Cu(p,x)^{60}Co – Cumulative
Empire-3.2.3
CoH-3.5.3
TALYS-1.8
TENDL-2017
ALICE-2017
A.Gruetter (1982)
L.Greenwood (1984)
S.Mills (1992)
R.Michel (1997)
M.Shahid (2015)
E.Garrido (2016)
S.Graves (2016)
A.Voyles (2018)
This Work
Cross Section (mb)
Proton Energy (MeV)

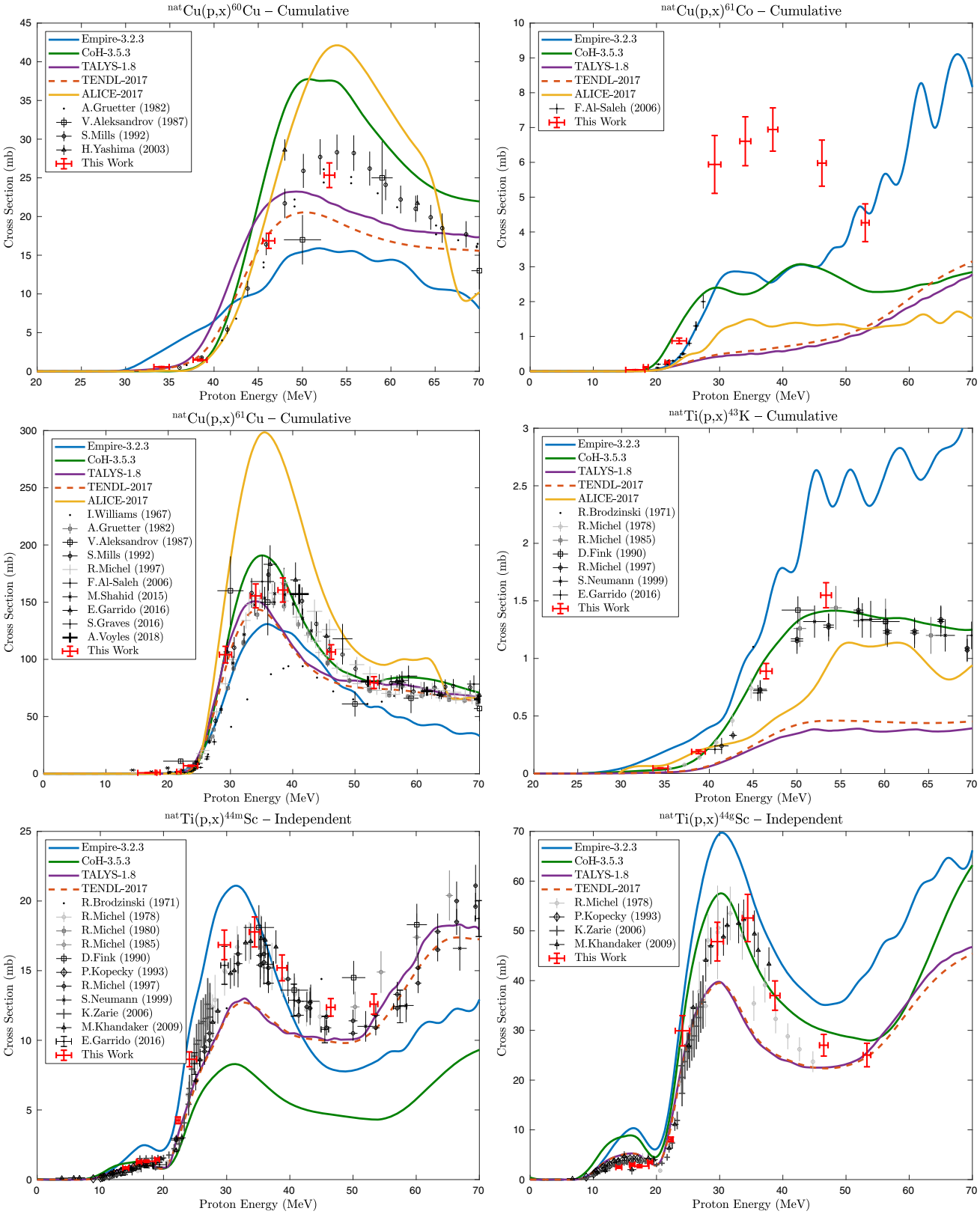
natCu(p,x)60Cu – Cumulative
Empire-3.2.3
CoH-3.5.3
TALYS-1.8
TENDL-2017
ALICE-2017
A.Gruetter (1982)
V.Aleksandrov (1987)
S.Mills (1992)
H.Yashima (2003)
This Work
Cross Section (mb)
Proton Energy (MeV)
natCu(p,x)61Co – Cumulative
Empire-3.2.3
CoH-3.5.3
TALYS-1.8
TENDL-2017
ALICE-2017
F.Al-Saleh (2006)
This Work
Cross Section (mb)
Proton Energy (MeV)
natCu(p,x)61Cu – Cumulative
Empire-3.2.3
CoH-3.5.3
TALYS-1.8
TENDL-2017
ALICE-2017
I.Williams (1967)
A.Gruetter (1982)
V.Aleksandrov (1987)
S.Mills (1992)
R.Michel (1997)
F.Al-Saleh (2006)
M.Shahid (2015)
E.Garrido (2016)
S.Graves (2016)
A.Voyles (2018)
This Work
Cross Section (mb)
Proton Energy (MeV)
natTi(p,x)43K – Cumulative
Empire-3.2.3
CoH-3.5.3
TALYS-1.8
TENDL-2017
ALICE-2017
R.Brodzinski (1971)
R.Michel (1978)
R.Michel (1985)
D.Fink (1990)
R.Michel (1997)
S.Neumann (1999)
E.Garrido (2016)
This Work
Cross Section (mb)
Proton Energy (MeV)
natTi(p,x)44mSc – Independent
Empire-3.2.3
CoH-3.5.3
TALYS-1.8
TENDL-2017
R.Brodzinski (1971)
R.Michel (1978)
R.Michel (1980)
R.Michel (1985)
D.Fink (1990)
P.Kopecky (1993)
R.Michel (1997)
S.Neumann (1999)
K.Zarie (2006)
M.Khandaker (2009)
E.Garrido (2016)
This Work
Cross Section (mb)
Proton Energy (MeV)
natTi(p,x)44gSc – Independent
Empire-3.2.3
CoH-3.5.3
TALYS-1.8
TENDL-2017
R.Michel (1978)
P.Kopecky (1993)
K.Zarie (2006)
M.Khandaker (2009)
This Work
Cross Section (mb)
Proton Energy (MeV)

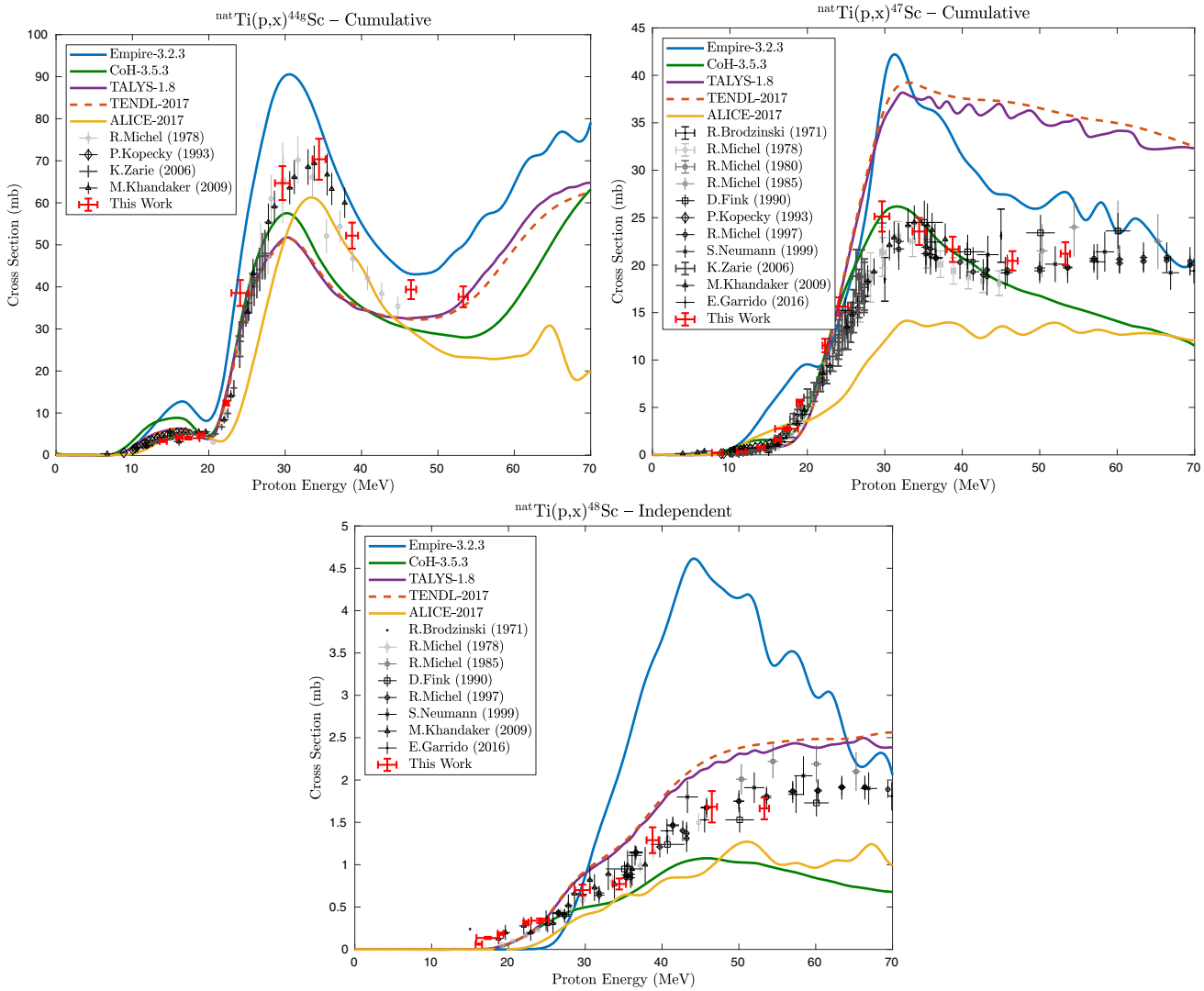

References

1. G.J. Topping, S. Paul, H. Cornelia, T. Ruth, S. Vesna, Med. Phys. **40**, 42502 (2013)
2. S.A. Graves, R. Hernandez, J. Fonslet, C.G. England, H.F. Valdovinos, P.A. Ellison, T.E. Barnhart, D.R. Elema, C.P. Theuer, W. Cai, R.J. Nickles, G.W. Severin, Bioconjug. Chem. **26**, 2118 (2015)
3. C.M. Lewis, S.A. Graves, R. Hernandez, H.F. Valdovinos, T.E. Barnhart, W. Cai, M.E. Meyerand, R.J. Nickles, M. Suzuki, Theranostics **5**, 227 (2015)
4. S.A. Graves, P.A. Ellison, H.F. Valdovinos, T.E. Barnhart, R.J. Nickles, J.W. Engle, Phys. Rev. C **96**, 014613 (2017)
5. A.L. Wooten, T.A. Aweda, B.C. Lewis, R.B. Gross, S.E. Lapi, PLoS One **12**, e0174351 (2017)
6. R. Hernandez, S.A. Graves, T. Gregg, H.R. VanDeusen, R.J. Fenske, H.N. Wienkes, C.G. England, H.F. Valdovinos, J.J. Jeffery, T.E. Barnhart, G.W. Severin, R.J. Nickles, M.E. Kimple, M.J. Merrins, W. Cai, Diabetes **66**, 2163 (2017)
7. S.A. Graves, P.A. Ellison, T.E. Barnhart, H.F. Valdovinos, E.R. Birnbaum, F.M. Nortier, R.J. Nickles, J.W. Engle, Nucl. Instrum Methods Phys. Res. Sect. B Beam Interact. Mater. Atoms **386**, 44 (2016)
8. Y. Dong, H. Junde, Nucl. Data Sheets **128**, 185 (2015)
9. J. Wang, X. Huang, Nucl. Data Sheets **144**, 1 (2017)
10. A. Voinov, E. Algin, U. Agvaanluvsan, T. Belgya, R. Chankova, M. Guttormsen, G.E. Mitchell, J. Rekstad, A. Schiller, S. Siem, Phys. Rev. Lett. **93**, 142504 (2004)
11. E. Algin, U. Agvaanluvsan, M. Guttormsen, A.C. Larsen, G.E. Mitchell, J. Rekstad, A. Schiller, S. Siem, A. Voinov, Phys. Rev. C **78**, 054321 (2008)
12. E. Algin, A. Schiller, A. Voinov, U. Agvaanluvsan, T. Belgya, L.A. Bernstein, C.R. Brune, R. Chankova, P.E. Garrett, S.M. Grimes, M. Guttormsen, M. Hjorth-Jensen, M.J. Hornish, C.W. Johnson, T. Massey, G.E. Mitchell, J. Rekstad, S. Siem, W. Younes, Phys. At. Nucl. **70**, 1634 (2007)
13. L.A. Bernstein, D.A. Brown, A.J. Koning, B.T. Rearden, C.E. Romano, A.A. Sonzogni, A.S. Voyles, W. Younes, Annu. Rev. Nucl. Part. Sci. **69**, 109 (2019)

14. S. Sudár, S.M. Qaim, Phys. Rev. C **73**, 34613 (2006)
15. N. Chakravarty, P.K. Sarkar, S. Ghosh, Phys. Rev. C **45**, 1171 (1992)
16. A.S. Voyles, L.A. Bernstein, E.R. Birnbaum, J.W. Engle, S.A. Graves, T. Kawano, A.M. Lewis, F.M. Nortier, Nucl. Instrum. Methods Phys. Res. Sect. B **429**, 53 (2018)
17. A. Springer, (2017). arXiv:1707.05908
18. M.K. Covo, R.A. Albright, B.F. Ninemire, M.B. Johnson, A. Hodgkinson, T. Loew, J.Y. Benitez, D.S. Todd, D.Z. Xie, T. Perry, L. Phair, K.P. Harrig, B.L. Goldblum, J.A. Brown, T. Laplace, J. Bevins, M. Harasty, E.F. Matthews, L.A. Bernstein, D.L. Bleuel, A. Bushmaker, in *2017 IEEE International Workshop on Metrology for AeroSpace (MetroAeroSpace)* (IEEE, 2017) pp. 484–488
19. J. Fitzgerald, FitzPeaks gamma analysis and calibration software (2009)
20. P.A. Aarnio, M.T. Nikkinen, J.T. Routti, J. Radioanal. Nucl. Chem. **248**, 371 (2001)
21. B. Singh, J. Chen, Nucl. Data Sheets **126**, 1 (2015)
22. J. Chen, B. Singh, J.A. Cameron, Nucl. Data Sheets **112**, 2357 (2011)
23. S.-C. Wu, Nucl. Data Sheets **91**, 1 (2000)
24. T.W. Burrows, Nucl. Data Sheets **108**, 923 (2007)
25. T.W. Burrows, Nucl. Data Sheets **107**, 1747 (2006)
26. T.W. Burrows, Nucl. Data Sheets **109**, 1879 (2008)
27. Y. Dong, H. Junde, Nucl. Data Sheets **121**, 1 (2014)
28. H. Junde, Nucl. Data Sheets **109**, 787 (2008)
29. H. Junde, H. Su, Y. Dong, Nucl. Data Sheets **112**, 1513 (2011)
30. M.R. Bhat, Nucl. Data Sheets **85**, 415 (1998)
31. C.D. Nesaraja, S.D. Geraedts, B. Singh, Nucl. Data Sheets **111**, 897 (2010)
32. E. Browne, J.K. Tuli, Nucl. Data Sheets **114**, 1849 (2013)
33. K. Zuber, B. Singh, Nucl. Data Sheets **125**, 1 (2015)
34. A.L. Nichols, B. Singh, J.K. Tuli, Nucl. Data Sheets **113**, 973 (2012)
35. B. Erjun, H. Junde, Nucl. Data Sheets **92**, 147 (2001)
36. B. Singh, Nucl. Data Sheets **108**, 197 (2007)
37. M.J. Berger, J.H. Hubbell, S.M. Seltzer, J. Chang, J.S. Coursey, R. Sukumar, D.S. Zucker, K. Olsen, (2010). http://physics.nist.gov/xcom
38. H. Bateman, in Proc. Cambridge Philos. Soc **15**, 423–427 (1910)
39. J. Cetnar, Ann. Nucl. Energy **33**, 640 (2006)
40. A. Hermanne, A. Ignatyuk, R. Capote, B. Carlson, J. Engle, M. Kellett, T. Kibédi, G. Kim, F. Kondev, M. Hussain, O. Lebeda, A. Luca, Y. Nagai, H. Naik, A. Nichols, F. Nortier, S. Suryanarayana, S. Takács, F. Tárkányi, M. Verpelli, Nucl. Data Sheets **148**, 338 (2018)
41. H.H. Andersen, J.F. Ziegler, *Hydrogen Stopping Powers and Ranges in all Elements* (Pergamon Press, New York, 1977)
42. J.F. Ziegler, J.P. Biersack, "The Stopping and Range of Ions in Matter", in *Treatise on Heavy-Ion Science: Volume 6: Astrophysics, Chemistry, and Condensed Matter*, edited by D. A. Bromley (Springer US, Boston, MA, 1985) pp. 93–129
43. J.F. Ziegler, J. Appl. Phys. **85**, 1249 (1999)
44. T. Böhlen, F. Cerutti, M. Chin, A. Fassò, A. Ferrari, P. Ortega, A. Mairani, P. Sala, G. Smirnov, V. Vlachoudis, Nucl. Data Sheets **120**, 211 (2014)
45. P.J. Huber, in *Proceedings of the fifth Berkeley symposium on mathematical statistics and probability*, Vol. 1 (University of California Press, 1967) pp. 221–233
46. M.B. Fox, A.S. Voyles, J.T. Morrell, L.A. Bernstein, A.M. Lewis, A.J. Koning, J.C. Batchelder, E.R. Birnbaum, C.S. Cutler, D.G. Medvedev, Phys. Rev. C **103**, 034601 (2021)
47. M. Herman, R. Capote, B.V. Carlson, P. Obložinský, M. Sin, A. Trkov, H. Wienke, V. Zerkin, Nucl. Data Sheets **108**, 2655 (2007)
48. A. Koning, J. Delaroche, Nucl. Phys. A **713**, 231 (2003)
49. M. Avrigeanu, A. Obreja, F. Roman, V. Avrigeanu, W. von Oertzen, At. Data Nucl. Data Tables **95**, 501 (2009)
50. T. Belgya, O. Bersillon, R. Capote Noy, T. Fukahori, G. Zhigang, S. Goriely, M. Herman, A.V. Ignatyuk, S. Kailas, A.J. Koning, P. Oblozinsky, V. Plujko, P.G. Young (IAEA, 2006)
51. A. D'Arrigo, G. Giardina, M. Herman, A.V. Ignatyuk, A. Taccone, J. Phys. G: Nucl. Part. Phys. **20**, 365 (1994)
52. A.J. Koning, D. Rochman, Nucl. Data Sheets **113**, 2841 (2012)
53. A. Gilbert, A.G.W. Cameron, Can. J. Phys. **43**, 1446 (1965)
54. T. Kawano, Los Alamos National Laboratory, unpublished (2003)
55. T. Kawano, P. Talou, M.B. Chadwick, T. Watanabe, J. Nucl. Sci. Technol. **47**, 462 (2010)
56. V. Avrigeanu, P.E. Hodgson, M. Avrigeanu, Phys. Rev. C **49**, 2136 (1994)
57. M. Blann, Phys. Rev. C **54**, 1341 (1996)
58. A. Nadasen, P. Schwandt, P.P. Singh, W.W. Jacobs, A.D. Bacher, P.T. Debevec, M.D. Kaitchuck, J.T. Meek, Phys. Rev. C **23**, 1023 (1981)
59. T.D. Thomas, Phys. Rev. **116**, 703 (1959)
60. B.L. Berman, S.C. Fultz, Rev. Mod. Phys. **47**, 713 (1975)
61. S.K. Kataria, V.S. Ramamurthy, S.S. Kapoor, Phys. Rev. C **18**, 549 (1978)
62. S. Kataria, V. Ramamurthy, M. Blann, T. Komoto, Nucl. Instrum. Methods Phys. Res. Sect. A: Accelerat. Spectrom. Detect. Associat. Equip.**288**, 585 (1990)
63. N. Otuka, S. Takács, Radiochim. Acta **103**, 1 (2015)
64. N. Otuka, E. Dupont, V. Semkova, B. Pritychenko, A.I. Blokhin, M. Aikawa, S. Babykina, M. Bossant, G. Chen, S. Dunaeva, R.A. Forrest, T. Fukahori, N. Furutachi, S. Ganesan, Z. Ge, O.O. Gritzay, M. Herman, S. Hlavač, K. Kato, B. Lalremruata, Y.O. Lee, A. Makinaga, K. Matsumoto, M. Mikhaylyukova, G. Pikulina, V.G. Pronyaev, A. Saxena, O. Schwerer, S.P. Simakov, N. Soppera, R. Suzuki, S. Takács, X. Tao, S. Taova, F. Tárkányi, V.V. Varlamov, J. Wang, S.C. Yang, V. Zerkin, Y. Zhuang, Nucl. Data Sheets **120**, 272 (2014)
65. V.N. Levkovski, (1991)
66. A. Klein, F. Rösch, S.M. Qaim, Radiochim. Acta **88**, 253 (2000)
67. I. Barchuk, V. Bulkin, V. Kuzmenkova, P. Kurilo, Y. Lobach, A. Ogorodnik, V. Procopenko, V. Sklyarenko, V. Tokarevsky, Atomnaya Ehnergiya **63**, 30 (1987)
68. M. Lagunas-Solar, J. Jungerman, Int. J. Appl. Radiat. Isot. **30**, 25 (1979)
69. I.R. Williams, C.B. Fulmer, Phys. Rev. **162**, 1055 (1967)
70. A.L. Wooten, B.C. Lewis, S.E. Lapi, Appl. Radiat. Isot. **96**, 154 (2015)
71. P. Bläuenstein, R. Pellikka, P. August Schubiger, Appl. Radiat. Isotopes **48**, 1097 (1997)
72. H. Thisgaard, M.L. Olesen, J.H. Dam, J. Labelled Compd. Radiopharm. **54**, 758 (2011a)
73. M.R. Zaman, S.M. Qaim, Radiochim. Acta **75**, 59 (1996)
74. A. Hermanne, M. Sonck, S. Takács, F. Tárkányi, Nucl. Instr. Methods Phys. Res. Sect. B: Beam Interact. Mater. Atoms **161**, 178 (2000)
75. H. Thisgaard, D. Elema, M. Jensen, Med. Phys. **38**, 4535 (2011b)
76. H. Valdovinos, R. Hernandez, S. Graves, P. Ellison, T. Barnhart, C. Theuer, J. Engle, W. Cai, R. Nickles, Appl. Radiat. Isot. **130**, 90 (2017)
77. H. Thisgaard, B.B. Olsen, J.H. Dam, P. Bollen, J. Mollenhauer, P.F. Hoilund-Carlsen, J. Nucl. Med. **55**, 1311 (2014)
78. N.C. Schoen, G. Orlov, R.J. McDonald, Phys. Rev. C **20**, 88 (1979)
79. M.S. Basunia, J.T. Morrell, M.S. Uddin, A.S. Voyles, C.D. Nesaraja, L.A. Bernstein, E. Browne, M.J. Martin, S.M. Qaim, Phys. Rev. C **101**, 064619 (2020)
80. D. Bleuel, L. Bernstein, R. Marsh, J. Morrell, B. Rusnak, A. Voyles, Appl. Radiat. Isot. **170**, 109625 (2021)

81. J. Zweit, P. Carnochan, R. Goodall, R. Ott, J. Nuclear Biol. Med. (Turin, Italy, 1991) **38**, 18 (1994)
82. J. Zweit, Current directions in radiopharmaceutical research and development **47** (1996)
83. F. Rösch, R.P. Baum (Springer, Berlin, 2014) pp. 83–94
84. F. Szelecsényi, Z. Kovács, K. Suzuki, K. Okada, T.N. van der Walt, G.F. Steyn, S. Mukherjee, J. Radioanal. Nucl. Chem. **263**, 539 (2005a)
85. T. Fukumura, K. Okada, F. Szelecsényi, Z. Kovács, K. Suzuki, Radiochim. Acta **92**, 209 (2004)
86. M.R. Lewis, M. Wang, D.B. Axworthy, L.J. Theodore, R.W. Mallet, A.R. Fritzberg, M.J. Welch, C.J. Anderson, J. Nucl. Med. **44**, 1284 (2003)
87. R.P. Bandari, Z. Jiang, T.S. Reynolds, N.E. Bernskoetter, A.F. Szczodroski, K.J. Bassuner, D.L. Kirkpatrick, T.L. Rold, G.L. Sieckman, T.J. Hoffman, J.P. Connors, C.J. Smith, Nucl. Med. Biol. **41**, 355 (2014)
88. E. Gourni, L. Del Pozzo, E. Kheirallah, C. Smerling, B. Waser, J.-C. Reubi, B.M. Paterson, P.S. Donnelly, P.T. Meyer, H.R. Maecke, Mol. Pharm. **12**, 2781 (2015)
89. F. Szelecsényi, G. Blessing, S. Qaim, Appl. Radiat. Isot. **44**, 575 (1993)
90. M. Aslam, S. Sudár, M. Hussain, A.A. Malik, H.A. Shah, S.M. Qaim, Radiochim. Acta **97**, 669 (2009)
91. K. Hilgers, T. Stoll, Y. Skakun, H. Coenen, S. Qaim, Appl. Radiat. Isot. **59**, 343 (2003)
92. F. Szelecsényi, G. Steyn, Z. Kovács, C. Vermeulen, N. van der Meulen, S. Dolley, T. van der Walt, K. Suzuki, K. Mukai, Nucl. Instrum. Methods Phys. Res. Sect. B **240**, 625 (2005b)
93. A. Voyles, M. Basunia, J. Batchelder, J. Bauer, T. Becker, L. Bernstein, E. Matthews, P. Renne, D. Rutte, M. Unzueta, K. van Bibber, Nucl. Instrum. Methods Phys. Res. Sect. B **410**, 230 (2017)
94. C. Muller, M. Bunka, J. Reber, C. Fischer, K. Zhernosekov, A. Turler, R. Schibli, J. Nucl. Med. **54**, 2168 (2013)
95. D.V. Filosofov, N.S. Loktionova, F. Rösch, Radiochim. Acta **98**, 149 (2010)
96. S.M. Qaim, R. Capote, F. Tarkanyi, *IAEA Technical Reports Series*, Tech. Rep. 473 (International Atomic Energy Agency, 2011)
97. C. Müller, M. Bunka, S. Haller, U. Köster, V. Groehn, P. Bernhardt, N. van der Meulen, A. Türler, R. Schibli, J. Nucl. Med. **55**, 1658 (2014)
98. L. Deilami-nezhad, L. Moghaddam-Banaem, M. Sadeghi, M. Asgari, Appl. Radiat. Isot. **118**, 124 (2016)
99. A.S. Voyles, Proton-induced reactions on Fe, Cu, & Ti from threshold to 55 MeV (2020)
100. M. Al-Abyad, M. Comsan, S. Qaim, Appl. Radiat. Isot. **67**, 122 (2009)
101. F. Al-Saleh, A. Al-Harbi, A. Azzam, Excitation functions of proton induced nuclear reactions on natural copper using a medium-sized cyclotron (2006)
102. V.N. Aleksandrov, M.P. Semenova, V.G. Semenov, Sov. Atom. Energy **62**, 478 (1987)
103. J. Barrandon, J. Debrun, A. Kohn, R. Spear, Nucl. Instrum. Methods **127**, 269 (1975)
104. A. Belhout, J. Kiener, A. Coc, J. Duprat, C. Engrand, C. Fitoussi, M. Gounelle, A. Lefebvre-Schuhl, N. de Séréville, V. Tatischeff, J.-P. Thibaud, M. Chabot, F. Hammache, H. Benhabiles-Mezhoud, Phys. Rev. C **76**, 034607 (2007)
105. R.L. Brodzinski, L.A. Rancitelli, J.A. Cooper, N.A. Wogman, Phys. Rev. C **4**, 1257 (1971a)
106. R.L. Brodzinski, L.A. Rancitelli, J.A. Cooper, N.A. Wogman, Phys. Rev. C **4**, 1250 (1971b)
107. E. Daum, Fed Rep Germ Rep **43** (1997)
108. F. Ditrói, F. Tarkanyi, J. Csikai, M.S. Uddin, M. Hagiwara, M. Baba, in *AIP Conference Proceedings*, Vol. 769 (AIP, 2005) pp. 1011–1014
109. D. Fink, J. Sisterson, S. Vogt, G. Herzog, J. Klein, R. Middleton, A. Koehler, A. Magliss, Nucl. Instrum. Methods Phys. Res. Sect. B **52**, 601 (1990)
110. E. Garrido, C. Duchemin, A. Guertin, F. Haddad, N. Michel, V. Métivier, Nucl. Instrum. Methods Phys. Res. Sect. B **383**, 191 (2016)
111. L.R. Greenwood, R.K. Smither, U.S. Dept, of Energy. Fusion Energy Series **18**, 11 (1984)
112. A. Grütter, Nucl. Phys. A **383**, 98 (1982)
113. P. Jung, J. Nucl. Mater. **144**, 43 (1987)
114. M.U. Khandaker, K. Kim, M.W. Lee, K.S. Kim, G.N. Kim, Y.S. Cho, Y.O. Lee, Appl. Radiat. Isot. **67**, 1348 (2009)
115. K. Kim, M.U. Khandaker, H. Naik, G. Kim, Nucl. Instrum. Methods Phys. Res. Sect. B **322**, 63 (2014)
116. P. Kopecky, F. Szelecsényi, T. Molnár, P. Mikecz, F. Tárkányi, Appl. Radiat. Isot. **44**, 687 (1993)
117. R. Michel, R. Bodemann, H. Busemann, R. Daunke, M. Gloris, H.-J. Lange, B. Klug, A. Krins, I. Leya, M. Lüpke, S. Neumann, H. Reinhardt, M. Schnatz-Büttgen, U. Herpers, T. Schiekel, F. Sudbrock, B. Holmqvist, H. Condé, P. Malmborg, M. Suter, B. Dittrich-Hannen, P.-W. Kubik, H.-A. Synal, D. Filges, Nucl. Instrum. Methods Phys. Res. Sect. B **129**, 153 (1997)
118. R. Michel, G. Brinkmann, H. Weigel, W. Herr, Nucl. Phys. A **322**, 40 (1979)
119. R. Michel, G. Brinkmann, J. Radioanal. Chem. **59**, 467 (1980)
120. R. Michel, G. Brinkmann, H. Weigel, W. Herr, J. Inorg. Nucl. Chem. **40**, 1845 (1978)
121. R. Michel, F. Peiffer, R. Stück, Nucl. Phys. A **441**, 617 (1985)
122. S.J. Mills, G.F. Steyn, F.M. Nortier, Int. J. Radiat. Appl. Instrum. Part A. Appl. Radiat. Isot. **43**, 1019 (1992)
123. S. Neumann, *Activation experiments with medium-energy neutrons and the production of cosmogenic nuclides in extraterrestrial matter.* Ph.D. thesis, Universität Hannover (1999)
124. M. Shahid, K. Kim, H. Naik, M. Zaman, S.-C. Yang, G. Kim, Nucl. Instrum. Methods Phys. Res. Sect. B **342**, 305 (2015)
125. S. Sudár, S.M. Qaim, Phys. Rev. C **50**, 2408 (1994)
126. S. Takács, L. Vasváry, F. Tárkányi, Nucl. Instrum. Methods Phys. Res. Sect. B **89**, 88 (1994)
127. H. Yashima, Y. Uwamino, H. Iwase, H. Sugita, T. Nakamura, S. Ito, A. Fukumura, Measurement and calculation of radioactivities of spallation products by high-energy heavy ions (2003)
128. K. Zarie, N. Al-Hammad, A. Azzam, Radiochim. Acta **94**, 795 (2006)
129. W. Zhao, H. Lu, W. Yu, Chin. J. Nucl. Phys. **15**, 337 (1993)